Icarus 216 (2011) 292–308

Contents lists available at SciVerse ScienceDirect

Icarus

journal homepage: www.elsevier.com/locate/icarus

Waves in Cassini UVIS stellar occultations 2. The C ring

Kévin Baillié [a,*], Joshua E. Colwell [a], Jack J. Lissauer [b], Larry W. Esposito [c], Miodrag Sremčević [c]

[a] Department of Physics, University of Central Florida, Orlando, FL 32816-2385, USA
[b] Space Sciences & Astrobiology Division, MS 245-3, NASA Ames Research Center, Moffett Field, CA 94035, USA
[c] LASP, University of Colorado, Boulder, CO 80309-0392, USA

ARTICLE INFO

Article history:
Received 1 December 2010
Revised 6 May 2011
Accepted 13 May 2011
Available online 30 May 2011

Keywords:
Saturn, Rings

ABSTRACT

We performed a complete wavelet analysis of Saturn's C ring on 62 stellar occultation profiles. These profiles were obtained by Cassini's Ultraviolet Imaging Spectrograph High Speed Photometer. We used a WWZ wavelet power transform to analyze them. With a co-adding process, we found evidence of 40 wavelike structures, 18 of which are reported here for the first time. Seventeen of these appear to be propagating waves (wavelength changing systematically with distance from Saturn). The longest new wavetrain in the C ring is a 52-km-long wave in a plateau at 86,397 km. We produced a complete map of resonances with external satellites and possible structures rotating with Saturn's rotation period up to the eighth order, allowing us to associate a previously observed wave with the Atlas 2:1 inner Lindblad resonance (ILR) and newly detected waves with the Mimas 6:2 ILR and the Pandora 4:2 ILR. We derived surface mass densities and mass extinction coefficients, finding $\sigma = 0.22(\pm0.03)$ g cm^{-2} for the Atlas 2:1 ILR, $\sigma = 1.31(\pm0.20)$ g cm^{-2} for the Mimas 6:2 ILR, and $\sigma = 1.42(\pm0.21)$ g cm^{-2} for the Pandora 4:2 ILR. We determined a range of mass extinction coefficients ($\kappa = \tau/\sigma$) for the waves associated with resonances with $\kappa = 0.13$ (±0.03) to $0.28(\pm0.06)$ cm^2 g^{-1}, where τ is the optical depth. These values are higher than the reported values for the A ring (0.01–0.02 cm^2 g^{-1}) and the Cassini Division (0.07–0.12 cm^2 g^{-1} from Colwell et al. (Colwell, J.E., Cooney, J.H., Esposito, L.W., Sremčević, M. [2009]. Icarus 200, 574–580)). We also note that the mass extinction coefficient is probably not constant across the C ring (in contrast to the A ring and the Cassini Division): it is systematically higher in the plateaus than elsewhere, suggesting smaller particles in the plateaus. We present the results of our analysis of these waves in the C ring and estimate the mass of the C ring to be between$3.7(\pm0.9) \times 10^{16}$ kg and $7.9(\pm2.0) \times 10^{16}$ kg (equivalent to an icy satellite of radius between 28.0($\pm$2.3) km and 36.2($\pm$3.0) km with a density of 400 kg m^{-3}, close to that of Pan or Atlas). Using the ring viscosity derived from the wave damping length, we also estimate the vertical thickness of the C ring between 1.9($\pm$0.4) m and 5.6($\pm$1.4) m, comparable to the vertical thickness of the Cassini Division.

1. Introduction

Many of Saturn's moons have low order inner Lindblad resonances (ILRs) located in Saturn's rings that excite outwardly propagating spiral density waves (Goldreich and Tremaine, 1982; Shu, 1984). Although some of these resonances coincide with obvious wavelike features in the rings, it is not the case in general. Most waves discovered in the C ring in Voyager data and reported by Rosen et al. (1991a,b) have no known resonance association. Identification of wavelike structures in the C ring can now be performed with enhanced confidence using Cassini data, especially occultation data provided by Cassini UVIS with a spatial resolution close to 20 m. By combining dozens of Cassini UVIS occultations, we have identified more than 30 waves in the C ring. We tentatively associate 3 of these waves (plus 2 others already known) with resonances, though a definitive association is complicated by uncertainties in the geometry of the occultations that are comparable to the wavelengths of many of the waves.

Many similar studies have been conducted on other parts of the rings and have mainly revealed longer waves than the ones we report here (Esposito et al., 1998, Spilker et al., 2004, Tiscareno et al., 2007 and references therein). The UVIS stellar occultations can resolve wave structures with short wavelengths, and the large number of occultations boosts the signal to noise ratio making it possible to combine profiles to identify waves with small amplitudes. Identifying the resonance locations is crucial prior to making associations with observed wavelike features. If the wave can be positively identified as a density or bending

* Corresponding author. Fax: +1 407 823 5112.
E-mail address: kevin.baillie@univ-paris-diderot.fr (K. Baillié).

0019-1035/$ - see front matter © 2011 Published by Elsevier Inc.
doi:10.1016/j.icarus.2011.05.019

wave associated with a specific resonance, the dispersion of the wave can be analyzed to constrain the surface mass density, σ, and mass extinction coefficient, $\kappa = \tau/\sigma$, where τ is the optical depth of the ring at the location of the wave. Rosen and Lissauer (1988) and Rosen et al. (1991b) provided estimates of the surface mass density in the C ring, together with constraints on the vertical thickness of the C ring from the damping length of the wave (less than 2.5 m). Tiscareno et al. (2007) derived surface mass density and ring thickness from Cassini ISS data (10–15 m in the inner A ring and 3–4.5 m in the Cassini Division). Colwell et al. (2009a) also analyzed high resolution Cassini UVIS data to determine the surface mass density and vertical thickness of the Cassini Division (3–6 m). These ring properties lead to a better understanding of the composition and size distribution of particles in the rings. Earlier analyses of density waves in the A ring and the Cassini Division have shown that κ is nearly constant across the A ring and into the Cassini Division ramp, and then jumps by a factor of $\sim$4 in the main Cassini Division, indicating a different particle population there (Colwell et al., 2009a). Tiscareno et al. (2009) analyzed the Iapetus -1:0 nodal bending wave and showed that the mass extinction coefficient drops by a factor of 10 between the main Cassini Division and the Cassini Division Ramp, and then jumps by a factor of 3 at the inner edge of the A ring.

The C ring shares similar optical depths and colors with the Cassini Division, however the strong satellite resonances are concentrated in the outer part of the ring system so that the same sort of systematic wave diagnostic applied there has not been possible in the C ring (or, for that matter, in the much more optically thick B ring). Here we show that the C ring has many wave-like structures throughout, and we identify several features not previously reported. Among them are what we believe to be density waves associated with the Mimas 4:1 ILR, Atlas 2:1 ILR, Mimas 6:2 ILR and Pandora 4:2 ILR, and a bending wave associated with the Titan -1:0 nodal resonance (Rosen and Lissauer, 1988). The majority of the wave features' locations, however, do not correspond in location to strong resonances with the known external satellites. Still, even in the absence of a resonance association, limits can be placed on both σ and κ from the measured dispersion of the wave within a multiplicative factor of the azimuthal parameter m, and by assuming that these features are in fact density or bending waves. In particular, we find $\sigma \geqslant 0.14\ \mathrm{g\,cm^{-2}}$ and $\kappa \leqslant 0.63\ \mathrm{cm^2\,g^{-1}}$. Besides these constraints, actual values of σ and κ were derived from resonance associations, defining a range of surface mass density from 0.22(±0.03) to 1.42(±0.21) g cm^{-2} and mass extinction coefficient from 0.13(±0.03) to 0.28(±0.06) cm^2 g^{-1}. These mass extinction coefficient values are higher than those found in the A ring (0.01–0.02 cm^2 g^{-1}) and in the Cassini Division (0.07–0.12 cm^2 g^{-1} from Colwell et al. (2009a)), implying smaller particle sizes in the C ring than either the A ring or the Cassini Division. We also estimate the mass of the C ring to be between $3.7(\pm0.9)\times10^{16}$ kg and $7.9(\pm2.0)\times10^{16}$ kg, equivalent to a Moon of 28.0(±2.3) km to 36.2(±3.0) km radius (a little larger than Pan or Atlas) with a density comparable to the two moons (400 kg m^{-3}). From the wave damping length and the ring viscosity, we also estimate the vertical thickness of the C ring to be between 1.9(±0.4) m and 5.6(±1.4) m, which is consistent with the vertical thickness of the Cassini Division (2–20 m) from Tiscareno et al. (2007) and Colwell et al. (2009a).

In Section 2 we describe occultation data provided by Cassini UVIS instrument. Section 3 reviews the principles of our analysis and presents newly identified waves. In Section 4 we show possible correlations with satellite resonance locations, and in Section 5, we estimate resulting physical properties of the rings at these locations.

2. Observations

We selected 62 complete or partial stellar occultations of the rings observed with the High Speed Photometer (HSP) of the Cassini Ultraviolet Imaging Spectrograph (UVIS) (Esposito et al., 1998, 2004; Colwell et al., 2010). These occultations, detailed in Table 1, have integration periods of 1–2 ms that provide a spatial resolution in the ring plane of about 10–20 m, varying with the viewing geometry (which varies between occultations and also within a given occultation). Occultations from 2007 and earlier are detailed in Colwell et al. (2007), and a description of calibration procedures applied to all occultations is presented in Colwell et al. (2010), which documents viewing geometries and star brightnesses. While some stars like γ Grus (Rev 40) are relatively faint, others such as β Centauri (Rev 64, 75, 77, 78, 81, 85, 89, 92, 96, 102, 104, 105) produce photon count rates 10–100 times higher. In addition, some stars have very low incidence angles relative to the plane of the rings, which allow for a better observation of structures inclined to the plane of the rings, such as bending waves. Direct measurements of the brightness of the occulted star are converted into an optical depth profile of the C ring. The high resolution of UVIS data allows us to distinguish small scale structures that are only a few kilometers in radial width with wavelengths that are a fraction of a kilometer. Fig. 1a shows an inward propagating wave (the wavelength decreases as the ring plane radius decreases), whereas Fig. 1b shows, in contrast, an outward propagating wave (i.e. a decreasing wavelength while ring plane radius increases).

3. Wavelet analysis

3.1. Wavelet transform

While looking at the raw data reveals evidence of several wave-like features, a more systematic process can be applied to the whole C ring in order to detect these periodic signatures, especially when the environment (gaps and ringlets, for example) prevents the signature from being obvious in the raw data. To this end, following the method detailed in Colwell et al. (2009a), we computed for each occultation a weighted wavelet Z (WWZ) transform, which is based on a Morlet wavelet transform (Torrence and Compo, 1998), and which can handle data with uneven positional sampling (Foster, 1996). For each subset of an occultation (typically 100 km in radial extent), we generate a wavelength power spectrum at each radial location (computed with 50 m resolution). Spatial wavelengths are distributed across 100 logarithmically-spaced bins between 0.3 km and 8 km (with a few exceptions that include wavelength powers outside these boundaries). In the next figures, we present WWZ wavelet power profiles, showing in the top panel the strength of spatial wavelength components as a function of ring plane radius, and in the bottom panel the corresponding raw data. Our data subsets extend well beyond the segments shown so our wavelet transforms are not affected by edge effects.

Not all individual occultation profiles present clear wave structures at the locations of wave structures seen in other occultations, mainly due to low signal rates, occultation elevation angle or slight radial shifts coming from navigation errors. These effects can be compensated for by co-adding all the wavelet transforms; this has the effect of enhancing any true periodic signature in the data, while random fluctuations will tend to average out (Colwell et al., 2009a). Because each of the individual occultations has uncertainties in the absolute geometry of about 1 km due primarily to uncertainties in the spacecraft's position along its trajectory, the co-adding process tends to smear the wave signal over this same 1 km range. When structures that are in the rings are clearly shifted in ring plane radius, we used circular fiduciary features

Table 1
Occultation summary.

Occultation Star (rev) side	Date (Year–Day)	$\|B\|$ (°)	ϕ (°)	R (km)	I_0 (Hz)
ξ 2 Cet (A) E	2004–280	14.9	72.9–89.4	57,757–80,239	1,300
126 Tau (8) E	2005–139	21.1	130.2–88.8	70,380–141,390	3,600
σ Sgr (11) I	2005–195	29.1	221.9–248.8	85,987–146,929	117,000
λ Cet (28) I	2006–256	15.3	304.0–258.5	74,330–144,011	2,500
α Sco B (29) I	2006–269	32.2	327.3–274.2	79,864–149,436	3,500
α Vir (30) I	2006–285	17.2	266.2–219.8	64,022–151,545	535,000
γ Lup (30) I	2006–286	47.4	157.1–185.9	83,062–94,587	80,000
γ Lup (30) E	2006–286	47.4	157.1–102.7	83,062–141,044	80,200
γ Lup (32) E	2006–313	47.4	26.3–38.2	84,310–136,192	74,200
α Ara (32) I	2006–314	54.4	280.9–276.5	61,333–139,786	38,900
α Ara (33) I	2006–325	54.4	280.8–276.6	65,886–145,356	38,700
α Vir (34) I	2006–337	17.2	282.1–220.9	74,536–153,654	506,000
α Vir (34) E	2006–337	17.2	282.1–344.6	74,536–160,059	516,000
κ Cen (35) E	2006–350	48.5	108.9–76.6	68,853–146,169	47,100
α Ara (35) I	2006–351	54.4	221.2–252.0	64,857–130,424	37,900
δ Per (36) E	2006–364	54,0	68.3–65.7	66,531–140,886	13,900
κ Cen (36) I	2007–002	48.5	250.0–237.8	63,531–156,380	44,200
ϵ Lup (36) E	2007–003	51,0	36.7–48.3	63,450–148,837	33,300
α Ara (36) I	2007–005	54.4	3.2–311.6	70,897–113,954	37,500
α Ara (36) E	2007–005	54.4	3.2–55.5	70,897–115,410	35,700
δ Per (37) I	2007–015	54,0	281.1–258.2	60,054–142,584	13,700
γ Ara (37) E	2007–022	61,0	142.5–117.2	80,500–155,599	27,300
γ Ara (38) I	2007–041	61,0	212.6–218.7	87,186–93,028	24,400
ϵ Psa (39) I	2007–045	23.7	255.0–277.4	86,910–94,013	2,500
ϵ Psa (39) E	2007–045	23.7	255.0–233.6	86,910–93,340	2,300
δ Per (39) I	2007–049	54,0	284.1–257.8	55,505–143,284	12,600
γ Gru (40) E	2007–063	61,0	232.3–181.8	67,340–147,704	7,500
θ Ara (41) E	2007–078	53.9	63.8–89.4	63,681–152,229	12,100
δ Per (41) I	2007–082	54,0	232.8–240.6	49,260–149,746	12,300
β Per (42) I	2007–098	47.4	227.8–230.8	84,461–149,674	19,700
ζ Ori (47) E	2007–179	2.66	99.4–106.6	78,770–137,732	175,000
ζ Cen (60) I	2008–060	53.6	221.1–231.2	66,648–146,507	107,000
δ Per (60) I	2008–062	54,0	283.9–274.5	54,975–146,216	11,600
ζ Cen (62) E	2008–082	53.6	77.3–67.0	63,689–145,087	107,000
α Ara (63) E	2008–092	54.4	95.8–112.3	73,261–141,566	2,900
γ Cas (64) I	2008–102	66.3	177.9–201.9	71,735–119,601	103,000
ϵ Cen (65) I	2008–110	59.6	221.7–229.0	69,876–148,192	130,000
β Cen (75) I	2008–188	66.7	283.5–264.4	72,427–144,448	592,000
β Cen (77) I	2008–202	66.7	282.9–264.4	73,334–144,893	583,000
β Cen (77) E	2008–203	66.7	34.6–54.4	73,267–143,444	604,000
β Cen (78) E	2008–210	66.7	23.7–54.8	58,470–145,023	572,000
β Cen (81) I	2008–231	66.7	294.4–267.6	72,829–151,692	546,000
β Cen (85) I	2008–260	66.7	295.3–269.5	73,112–143,414	531,000
β Cen (89) I	2008–290	66.7	296.4–269.8	71,854–141,886	500,000
α Cru (92) I	2008–312	68.2	125.0–181.6	77,557–155,730	516,000
β Cen (92) E	2008–313	66.7	42.7–59.1	50,676–154,574	463,000
β Cen (96) I	2008–343	66.7	288.6–264.8	72,456–155,341	441,000
δ Cen (98) I	2008–359	55.6	209.3–212.0	55,447–153,103	36,100
β Cru (98) I	2008–359	65.2	157.3–202.6	58,104–154,683	279,000
γ Cas (100) E	2009–015	66.3	86.4–66.0	72,440–140,370	56,000
β Cen (102) I	2009–031	66.7	250.7–248.3	73,243–143,508	369,000
β Cen (104) I	2009–053	66.7	179.2–220.0	70,203–147,291	365,000
β Cen (104) E	2009–053	66.7	134.8–94.7	68,934–131,988	365,000
β Cen (105) I	2009–065	66.7	199.1–222.0	88,502– 158,713	310,000
β Cen (105) E	2009–065	66.7	121.7–91.5	77,787–147,358	301,000
ζ Cen (112) I	2009–163	53.6	236.6–241.2	71,486–143,214	53,000
μ Cen (113) I	2009–177	48.7	236.2–240.6	75,975–155,785	9,400
α Lup (113) I	2009–178	53.8	172.4–217.8	83,839–118,956	26,400
α Lup (113) E	2009–178	53.8	172.4–160.9	83,839–85,541	26,400
σ Sgr (114) I	2009–198	29.1	332.1–329.2	84,449–149,875	33,300
μ Sgr (115) I	2009–212	24.9	44.1–27.4	90,967–94,935	>200+
μ Sgr (115) E	2009–212	24.9	44.1–80.3	90,967–112,618	>200+

Notes: Rev refers to the number of the orbit of Cassini around Saturn on which the observation occurred. Cassini revs are numbered 0, A, B, C, 3, 4, and consecutively thereafter. Ranges in ϕ and R are for the entire observation, and the range in ϕ is listed in the order corresponding to the range in R. In some cases, part of the occultation is obscured by the planet. The values listed here are for the full occultation, not just the part where the star is unobstructed. Durations indicate the time from the start of measurements to the last measurement, including gaps caused by data dropouts. +: Indicates occultations for which the stellar signal cannot be directly measured, and the values listed in the I_0 column are estimates from other occultations. I and E indicate ingress and egress occultations, respectively.

from French et al. (1993) to adjust the radial scale for those occultations. Nevertheless, those edge locations are not precise to better than 1 km, so we are left with a typical uncertainty in ring plane radius of 1 km.

We found that once a wave has been identified, the most precise information can be extracted from the occultations presenting the highest photon count rates – the 12 occultations of β Centauri, the α Virginis rev. 30 and 34 occultations and the ζ Orionis rev. 47

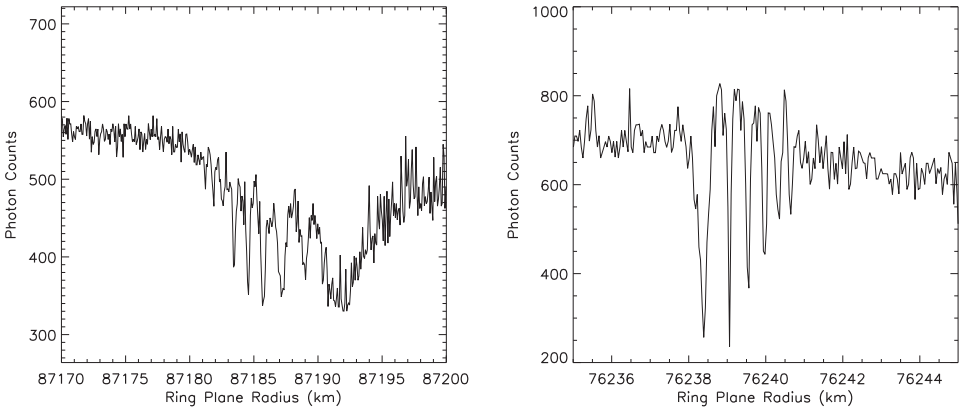

Fig. 1. Photon counts from the occultation of β Centauri (Rev 75) showing structure 32 propagating inward (left), and of α Virginis (Rev 34) showing feature 6 propagating outward (right).

occultation (Table 1)). The β Centauri occultations have a high elevation angle ($B = 66.7°$) relative to the ring plane and therefore allow us to identify the density wave positions particularly well, whereas the others have some of the lowest B angles, increasing the visibility of the bending waves.

Our WWZ analysis revealed the 10 waves reported by Rosen et al. (1991a,b), the 12 additional waves reported by Colwell et al. (2009b) including the Atlas 2:1 density wave at 87,645 km (structure 33), together with 18 previously unreported wavelike features, which appear to be propagating waves. We consider a wave to be potentially propagating if it exhibits a dispersion in wavelength (decreasing or increasing with distance from Saturn) analogous to density and bending waves.

In addition to 10 previously reported structures presenting a wavelength decreasing with radius, 11 previously known features with wavelength increasing with radius, and one last with no reported preferred direction of propagation, our new structures are divided between 12 new outward features, 5 new inward ones and one which direction of propagation is not clear. Occultation and wavelet profiles showing the propagation for selected structures are presented in Figs. 3–30. Outward propagating features are visible in both β Centauri and α Virginis occultations while inward structures are only visible in α Virginis and ζ Orionis occultations, suggesting that the former may be density waves and the latter may be bending waves, with external peturbers for both sets.

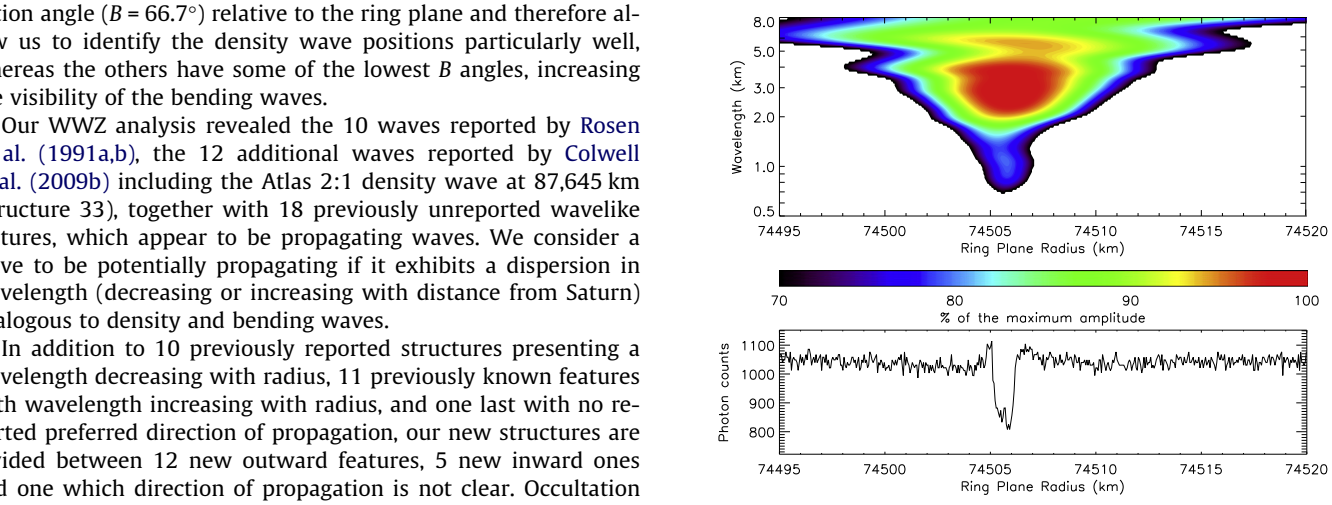

Fig. 3. WWZ wavelet power profile of embedded ringlet ER1 computed from 62 individual occultation profiles. Lower panel shows the β Centauri, rev. 85 occultation profile. Embedded ringlets produce this characteristic triangular profile in the power contour plots.

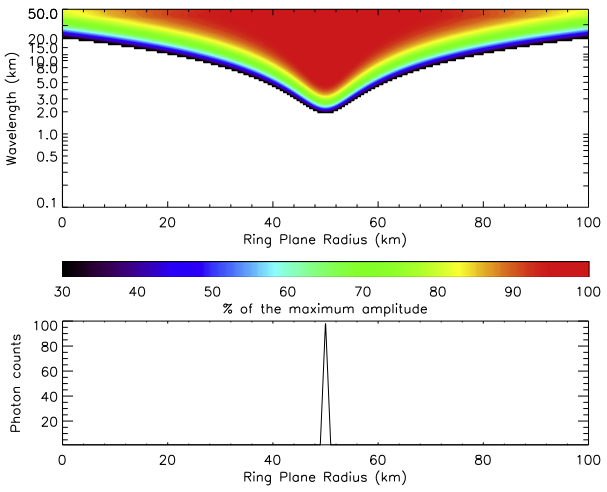

Fig. 2. WWZ wavelet power profile for a Dirac signal. The bottom panel presents the simulated data that were analyzed to produce these power transforms.

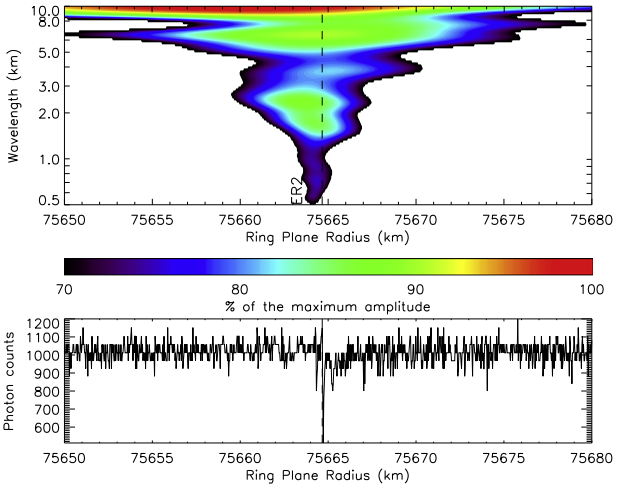

Fig. 4. Co-added WWZ wavelet power profile of embedded ringlet ER2, computed from individual occultation profiles. Lower panel shows the α Virginis, rev. 34 occultation profile. A clear triangular shape is visible as the resulting signature of embedded ringlet ER2.

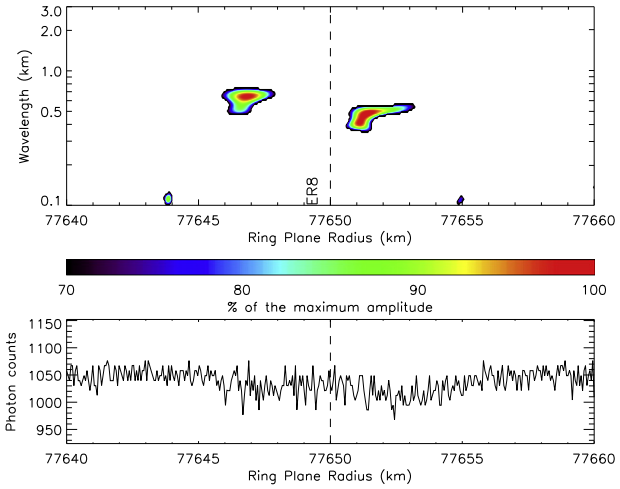

Fig. 5. Co-added WWZ wavelet power profile of embedded ringlet ER8, computed from individual occultation profiles. Lower panel shows the β Centauri, rev. 85 occultation profile. The double peaks, characteristic of ER8, present clear signatures.

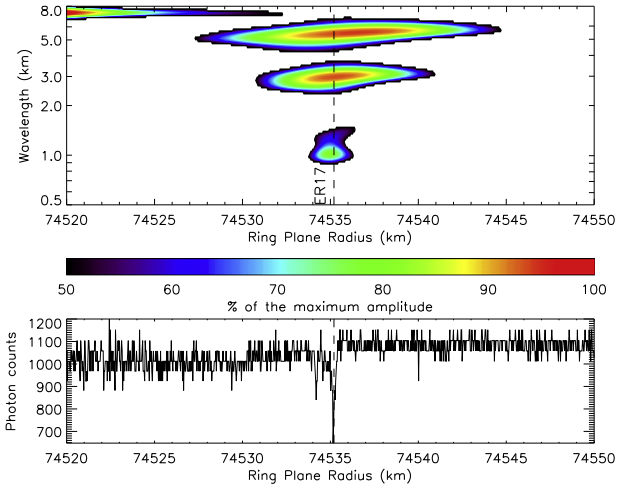

Fig. 6. Co-added WWZ wavelet power profile of embedded ringlet ER17, computed from individual occultation profiles. Lower panel shows the α Virginis, rev. 30 occultation profile. A clear triangular shape is visible as the resulting signature of embedded ringlet ER17.

3.2. Ringlet signatures

We observe a great variety of wavelet power signatures: from clearly propagating waves to triangle-shaped signatures produced by narrow ringlets. In order to better analyze the results of the wavelet profiles, we generated the profiles for some basic reference signals. A sine signal will obviously result in a constant profile at the wavelength of the signal. Ascending or descending isolated ramps will not show any specific wavelength, however step functions will radically change the profiles. In those cases we will find some power at wavelengths equal to the width of the step. This is confirmed for a more "Dirac"-like signal, that we can consider as a superposition of several step functions with decreasing width. Therefore, we expect to find a pattern of power at all wavelengths, centered on the Dirac peak location and with widths proportional to the wavelength. This would result in an inverted triangular shape of the wavelet profile (Fig. 2).

Signatures such as the latter for which we cannot positively identify a propagating wave on individual occultation scans, are listed in Table 2. For example, structure 1 of this table is displayed

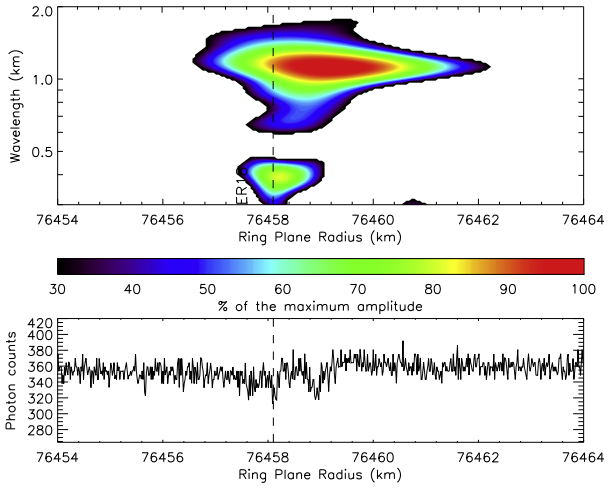

Fig. 7. Co-added WWZ wavelet power profile of embedded ringlet ER18, computed from individual occultation profiles. Lower panel shows the β Centauri, rev. 104 occultation profile. Two peaks, separated by 0.8 km, are visible on the occultation profile.

in Fig. 3: the location of this signature coincides with the Embedded Ringlet 1 reported by Colwell et al. (2009b). We cannot distinguish any propagating wave in any individual occultation at this radial position, and the signature is consistent with the triangle-shaped artifact generated by a "Dirac" signal, modeling an embedded ringlet. Other examples are observed at the positions of other embedded ringlets such as ER2 (Fig. 4) or ER8 (double peak) (Fig. 5). But we also observe such patterns at two locations where embedded ringlets were not previously reported. Individual occultation profiles at these positions confirm the existence of new embedded ringlets (ER17 (Fig. 6) and ER18 (Fig. 7) of Table 2). In these cases, the ring structure signature is dominant over a possible propagating wave, but that does not exclude the possibility that these structures themselves could be due to satellite resonances. Finally, some other known ringlets coincide with the location of some waves reported here: ER7 is just 3 km exterior to the inward propagating structure 5 in Table 3, ER10 is 4 km interior to the inward propagating structure 16 (Fig. 8), ER13 is overlapping with inward propagating structure 32 (Fig. 9) and ER16 is also overlapping with inward propagating features 38 and 39 (Fig. 10), and coincides with the location of Mimas 3:1 ILR. We notice that most of the embedded ringlets coincide with a wavelike signature that cannot be explained by the shape of the ringlet alone. For those signatures that appear to be propagating, the direction is apparently inward. Despite this direction of propagation, which would suggest that they are bending waves if due to external satellites, these waves are very clear on β Centauri occultations. This direction of propagation has been explained by Rosen and Lissauer (1988) and Nicholson et al. (2010), who give a detailed analysis of the Titan -1:0 nodal resonance that is an outward propagating bending wave, due to its negative pattern speed. We report only two potential resonance associations in the neighborhood of these ringlets: Pandora 2:1 ILR at 90,165.4 km and Mimas 3:1 ILR at 90,195.9 km are located inside ER16 and at its outer edge respectively.

3.3. Waves near known resonances

Some of the wavelet signatures we observe may be related to propagating waves, and we would expect some of these waves to be associated with particular satellite resonances. The direction of propagation is not always obvious on every reported signature:

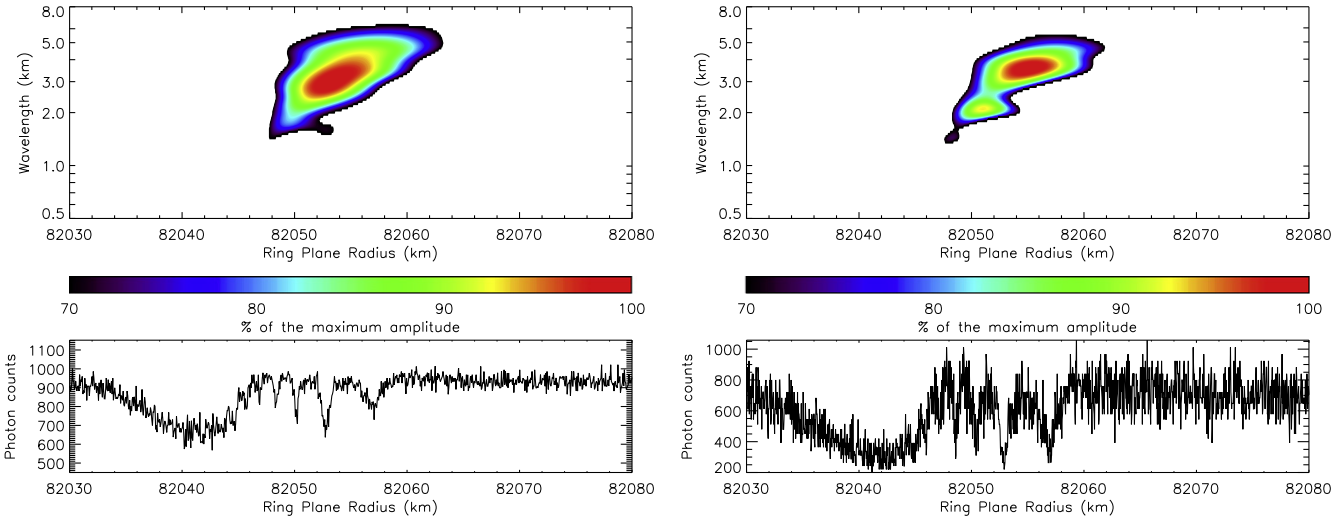

Fig. 8. WWZ wavelet power profile of structure 16, computed from co-added wavelet profiles of high-incidence angle occultations (left) and low-incidence angle occultations (right). Lower panels show the β Centauri, rev. 85 occultation profile (left) and the α Virginis, rev. 34 occultation profile (right). Structure 16 is located just exterior to the embedded ringlet ER10.

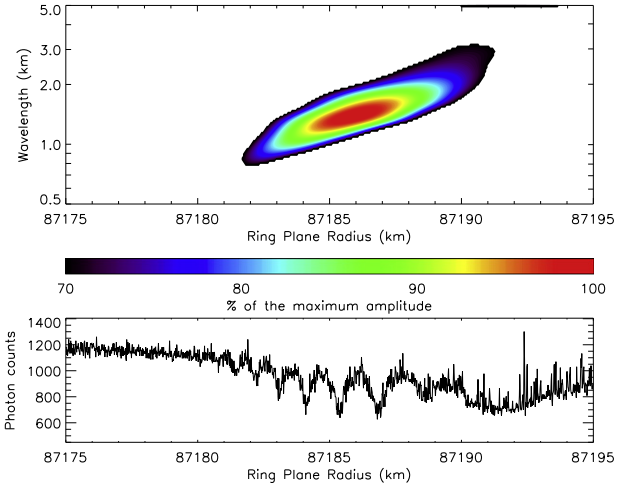

Fig. 9. Co-added WWZ wavelet power profile of structure 32, computed from individual occultation profiles. Lower panel shows the β Centauri, rev. 85 occultation profile. Structure 32 is coexisting with the embedded ringlet ER13 that spreads from 87,180 km to 87,210 km.

we observe that the directions derived from decreasing amplitude do not always confirm the direction of decreasing wavelength away from the wave starting point. We report the wavelike features in Table 3 with their radial extents as measured from the co-added wavelet profiles: we consider the borders of the structure to be delimited by the area where the wavelet power is higher than 85% of the maximum power of the structure. We also mention potential previous references and possible resonance associations, together with wave starting locations from our data (for the structures that present an actual chance of being waves). Using the known dispersion relation for the wave, we can extrapolate the position where the wavelength of maximum power is expected to diverge: this position will be referred to as the wave source location and is determined with a precision of the order of a few kilometers, depending on the precision of the wavelength fitting. The distance between these wave source locations and the theoretical resonance locations provides a good test of a resonance association with an observed wave. 33 out of 40 structures are narrower in radial extent than 13 km. Structure 27 (which is about 15 km wide) and structure 28 (with a width of about 52 km) are among the largest features. These waves are not apparent in the Voyager radio and stellar occultations due to their small amplitude and short wavelength. Details on particular waves are provided below.

- Around 74,891 km, we observe the superposition of a short propagating wave and a ringlet structure signature: the Mimas 4:1 inner Lindblad resonance (Fig. 11). This feature was identified by Rosen et al. (1991a), who used it to provide a wave-derived estimate of the C ring surface mass density ($\sigma \sim 1 \pm 0.5$ g cm^{-2}), as well as a lower bound on the C ring viscosity ($\nu \gtrsim 7.19 \times 10^{-5}$ cm^2 s^{-1}). We derive a consistent value of the surface mass density in that vicinity: $\sigma = 0.58$ (± 0.09) g cm^{-2}.
- Wave 12, presented in Fig. 12, matches the location of the Titan -1:0 nodal resonance, supposed to be located at 77,511.3 km, as reported in Rosen et al. (1991a) and analyzed in Rosen and Lissauer (1988). As we can see in Table 6, the resonant argument parameters prove that this resonance is an inner vertical resonance and therefore we expect to find a bending wave, even if it is propagating outward (since its pattern speed is negative). That vertical property is the reason why the wave is very clearly visible on the α Virginis, rev. 30, occultation. Titan also has another resonance in the C ring: an apsidal 1:0 resonance around 77,846 km, which is located in the Colombo Gap but which could be the origin of the ringlet in that gap (Lissauer and Cuzzi, 1982).
- Wave 33 (Fig. 13) appears to be associated with the Atlas 2:1 inner Lindblad resonance at 87,646.5 km. However, the dispersion of wave 33 is smaller than expected for the location of the Atlas 2:1 ILR making this association tentative.
- Wave 36 and 37 are separated by only 10 km (Fig. 14). These two waves are propagating outward and could be associated with resonances. Indeed, the 89,889 km wavetrain matches the Mimas 6:2 ILR at 89,883.3 km while the 89,900 km wave fits the Pandora 4:2 ILR which is located at 89,894.0 km. The Mimas 3:1 ILR is stronger than the Mimas 4:1 ILR and Mimas 6:2 ILR (Table 4). We would therefore expect to observe a clearer wave at its location around 90,195 km. This resonance location coincides with the outer edge of the embedded ringlet ER16 and with observed feature 39 (Fig. 10). However, this structure is not clearly propagating and we cannot derive physical properties of the ring from this feature. We would also expect to

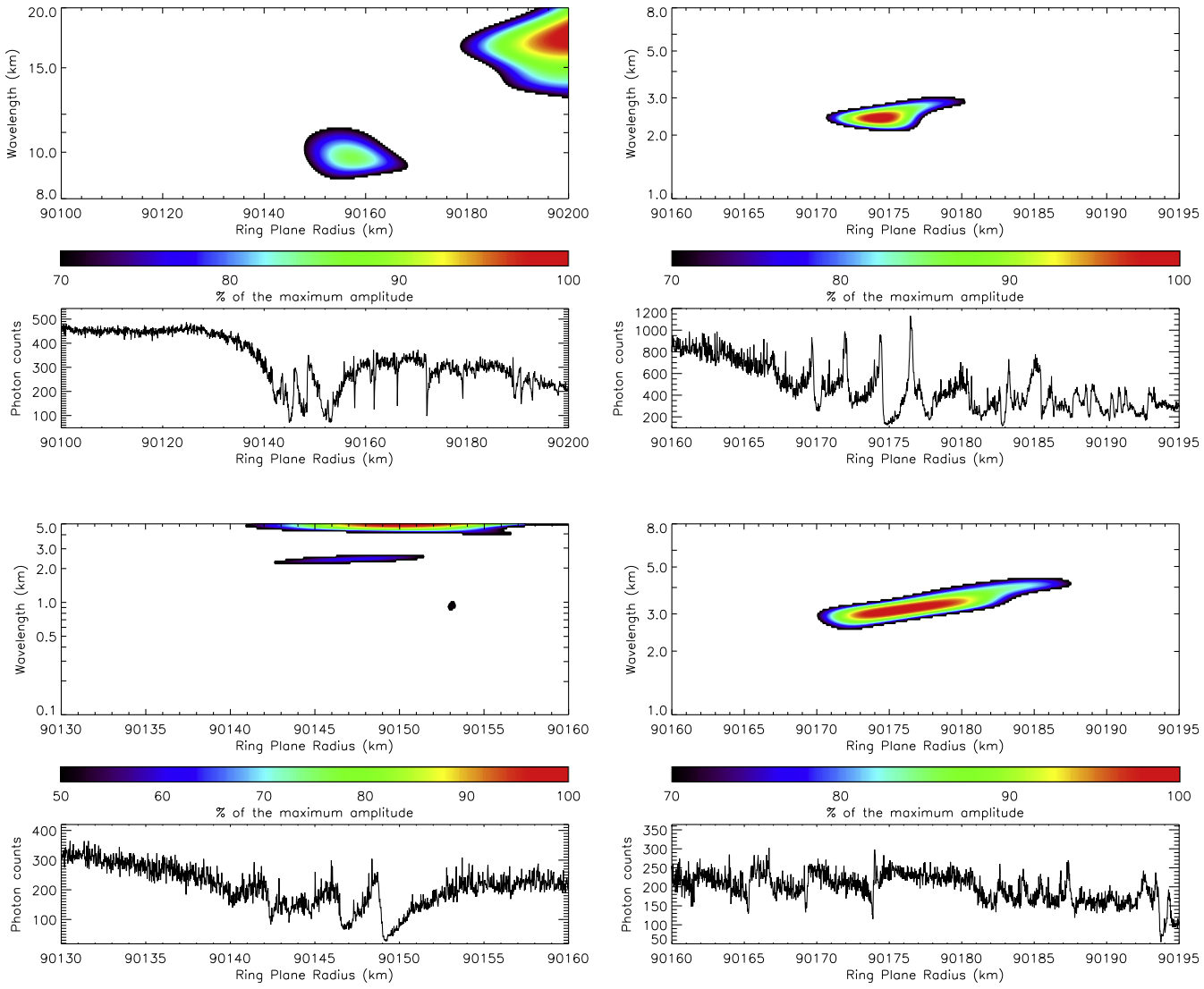

Fig. 10. WWZ wavelet power profile of the different parts composing structure 38, computed from individual occultation profile of β Centauri, rev. 89 (upper left), β Centauri, rev. 64 (upper right), and β Centauri, rev. 104 Ingress (bottom). The variety of observed patterns and the local superposition of waves at different wavelengths suggest that this is not a simple bending wave.

observe waves associated with the Pandora 2:1 ILR which is stronger than the Pandora 4:2 ILR. That wave would actually be located at 90,165 km, fitting the position of feature 38 (Fig. 10), close to the previously mentioned Mimas 3:1 ILR. Whether ER16 is created by this resonance or not, its presence prevents identification of any wave there. Pandora's orbit parameters being very similar to the ones of Prometheus, we can also expect to observe waves associated with Prometheus resonances. Feature 34 is actually very close to the Prometheus 2:1 ILR located at 88,712.9 km, in the ringlet R4 (Fig. 15). We observe periodic features in R4 but could not estimate a direction of propagation for this signal. The Prometheus 4:2 ILR is also located close to a ringlet (inner edge of ER15) around 88,298 km, while the Prometheus 4:2 IVR is at the outer edge of the Maxwell Ringlet (at 87,589 km). The presence of these embedded ringlets at the locations of resonances is suggestive of a causal link, but we can only point out the associations here. Nevertheless, it strengthens our confidence in the identification of waves 36 and 37 with the Mimas 6:2 ILR and Pandora 4:2 ILR that the stronger first-order counterparts of those resonances do have ring features associated with them.

3.4. Other wavelike signatures

3.4.1. Outward propagating signatures

Structures 3 and 4 are shown in Fig. 16. A 4 km wide embedded ringlet appears in β Centauri occultations and seems to disturb the region while the α Virginis signal is very clear. Our resonance catalog (Table 4) indicates that we should not expect many low order resonances at these locations in the C ring, and even the Daphnis 5:2 ILR at 74,923 km is quite far from feature 3 (12 km interior). Structures 7 and 8 (Fig. 17) appear to coexist around the same location as structure 9 (Fig. 18), though we cannot state that structures 7 and 8 are propagating like waves. Structure 24 (Fig. 19), from Colwell et al. (2009b), presents the peculiarity that it seems to propagate outward and yet it is only visible at low incidence angles, such as on ζ Orionis. Structure 27 (Fig. 20) is one of the most extended features that we observed in the C ring. This feature is clearly propagating outward. Yet, no low-order inner Lindblad resonance could be found in this neighborhood. Structure 28 (Fig. 21) is certainly the second-most extended one that we found in the C ring after the Titan -1:0 nodal resonance. This is a 52-km-long outward propagating wavetrain in the plateau P7 (Colwell et al.,

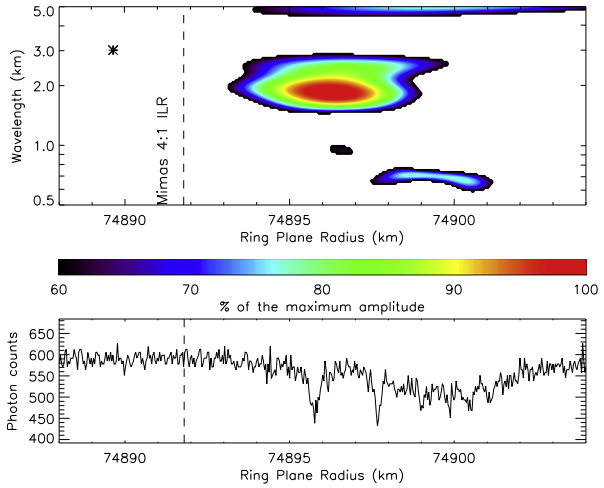

Fig. 11. WWZ wavelet power profile around the Mimas 4:1 inner Lindblad resonance (r_L = 74,891.9 km, marked by the vertical dashed line), computed from β Centauri, rev. 75 individual occultation profile. The possible superposition with a ringlet structure is disturbing our perception of the direction of propagation. The asterisk locates the position of the observed wave source.

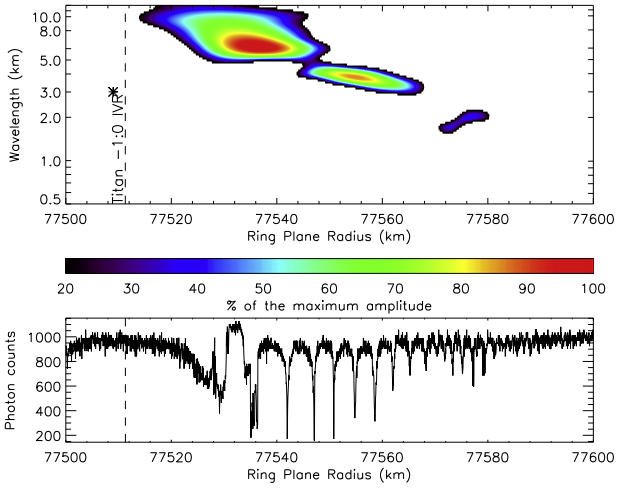

Fig. 12. WWZ wavelet power profile of wave 12, computed from α Virginis, rev. 34 individual occultation profile. Titan -1:0 nodal resonance at 77,511.3 km (vertical dashed line) excites an outward propagating wave. The asterisk locates the position of the observed wave source.

2009b) at 86,400 km. This feature is actually most prominent in UVIS occultations of stars at high incidence angle (large B angles, Table 1), suggesting that it is not a bending wave but instead represents variations in particle packing with radius like in a density wave. Still, no low-order resonance with any known moon is expected at the location of this wavetrain. The direction of propagation of feature 20 is not very clear, but appears to be outward from Fig. 22. The Pan 4:2 ILR at 84,814.5 km could be a match for that structure, which is 7 km exterior. However, the length of that distance, compared to the length of the structure itself, raises the concern of a chance association.

In order to estimate the chance of a coincidental match between a wave location and a resonance location, we performed the following simple statistical test. We estimate the probability p that drawing Q random numbers for r between 74,000 and 92,000 km, N of them show up within X km of one of the W nth-order resonances. N is the number of waves we associate with nth-order resonances and X is the radial separation between the starting point of a wave and the theoretical location of an nth-order resonance that we associate with that wave. We uniformly pick Q random positions in the range of width L. Considering one isolated pick, the probability that one random position is within X km of W specific positions is $\frac{2XW}{L}$. Considering Q picks, the probability $p'(i)$ that exactly i of them are within X km of W specific positions is

$$p'(i) = C_Q^i \left(\frac{2WX}{L}\right)^i \left(1 - \frac{2WX}{L}\right)^{(Q-i)} \quad (1)$$

Therefore, the probability p that at least N of them are within X km of W specific positions is

$$p = \sum_{i=N}^{Q} C_Q^i \left(\frac{2WX}{L}\right)^i \left(1 - \frac{2WX}{L}\right)^{(Q-i)} \quad (2)$$

where L = 92,000 − 74,000 km and Q = 40

Concerning the possible association of the Pan 4:2 inner Lindblad resonance with feature 20 (Fig. 23), we measure a wave source location at 84,775 ± 8 km (39.5 km interior to the resonance location). Our catalog of second-order inner Lindblad resonances in the C ring was narrowed to 14 potential resonances (W = 14). Therefore, the probability that a second-order inner Lindblad resonance will come within 39.5 km of one of the outward propagating waves is higher than 87%. This Pan 4:2 ILR association therefore does not appear to be reliable at all.

Finally, Tiscareno et al. (2007) already rejected the possible association of feature 40 with the Tethys 6:1 inner Lindblad resonance that would be the best candidate at 90,279.6 km (Fig. 24).

3.4.2. Inward propagating signatures

Structure 13 (Fig. 25) is clearly propagating inward both in the β Centauri and α Virginis occultations. Structure 15 (Fig. 26), from Colwell et al. (2009b), appears to propagate inward on every occultation. Structures 16 and 17 (Figs. 8 and 27), from Rosen et al. (1991a), also present inward propagation that is visible on both co-added profiles. Additionally, we notice in Fig. 8 the presence of a recurring hump interior to the feature. Structures 23 and 25, the former reported by Rosen et al. (1991a), are only seen in the small-incidence-angle occultation of ζ Orionis. This, combined with the inward direction of propagation, strongly indicates these could be bending waves. Structure 32 (Fig. 9) was reported by Colwell et al. (2009b) and propagates inward. Between 90,130 km and 90,200 km, we observe different features (gathered under structure 38) depending on the occultation (Fig. 10).

3.4.3. Other signatures

Structure 11 was reported by Colwell et al. (2009b) as an inward propagating feature. It appears to be located at the position of a 6-km-wide embedded ringlet that generated a wavelike signature around 12 km, but we can extract an actual feature at shorter wavelengths (Fig. 28). Although the amplitude of structure 11 decreases outward, the wavelength remains constant, and thus we cannot state the direction of propagation for that structure.

We see an inward-propagating structure in the well-known eccentric Maxwell Ringlet at 87,545 km (Figs. 29 and 30). With a different regularity, we observe wavelike signatures in the R4 ringlet at 88,700 km; Fig. 15 presents what could be interpreted as an inward propagating wave. We also notice that the Prometheus 2:1 ILR is located inside the R4 ringlet and that the Mimas 3:1 inner vertical resonance is located at 88,728.3 km, which is farther from the expected position of the wave than for the other associations previously made.

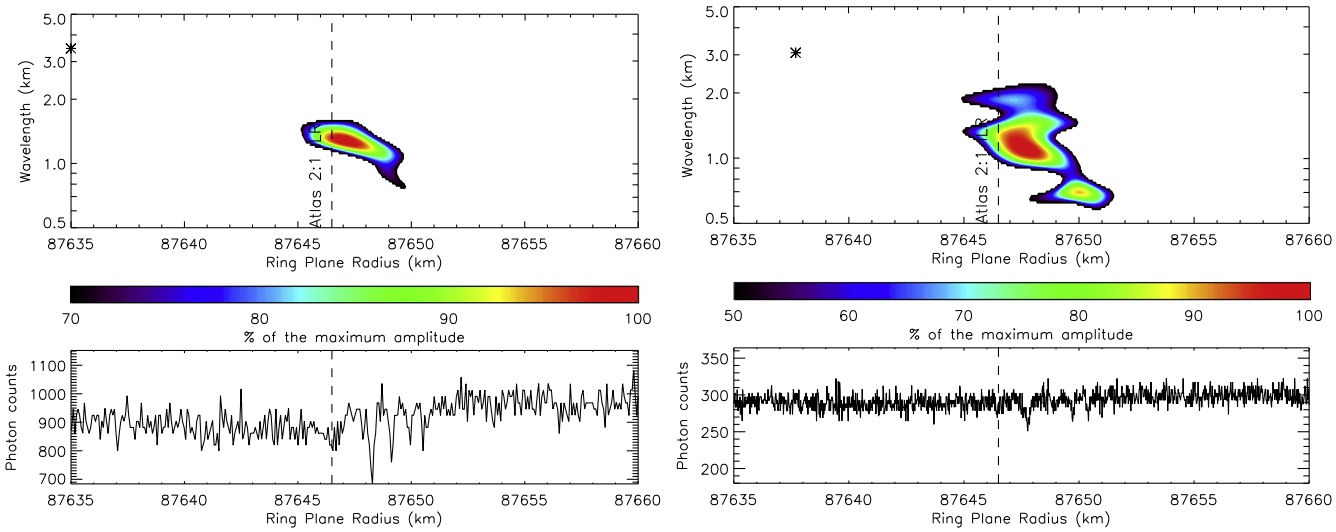

Fig. 13. WWZ wavelet power profile of wave 33, computed from α Virginis, rev. 34 (left) and β Centauri, rev. 105 (right) individual occultation profiles. The Atlas 2:1 ILR (at 87,646.5 km – vertical dashed line) has a greater torque than the Pan 2:1 ILR which does not seem to excite a wave at 85,105 km. The asterisks locate the positions of the observed wave sources. Profiles of this wave consistently show a dispersion that places the wave source several km interior to the wave feature and the theoretical location of the Atlas 2:1 ILR.

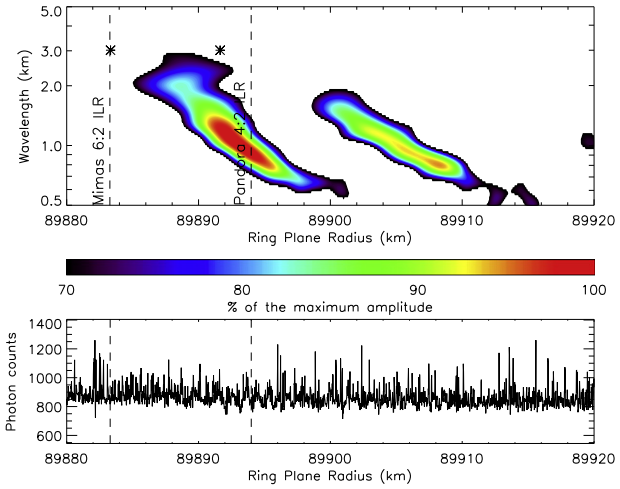

Fig. 14. Co-added WWZ wavelet power profile of waves 36 and 37, computed from co-added wavelet profiles. Mimas 6:2 ILR is at 89,883.3 km and Pandora 4:2 ILR is at 89,894.0 km, pointed by the vertical dashed lines. Lower panel shows the β Centauri, rev. 85 occultation profile. The almost 3:2 corotation resonance between Mimas and Pandora explains the proximity of these two waves. The asterisks locate the positions of the observed wave sources with uncertainties below 1 km.

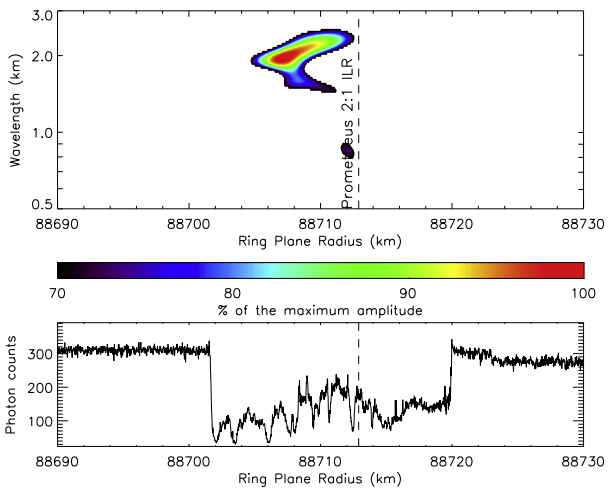

Fig. 15. WWZ wavelet power profile of R4 ringlet, computed from β Centauri, rev. 105 individual occultation profile. The Prometheus 2:1 ILR position is represented by a vertical dashed line.

4. Results

We produced a map of resonances with the known external perturbers (Section 4.1) up to order eight, allowing us to identify potential associations between waves and resonances such as the Pandora 4:2 ILR (Section 3 and summarized in Fig. 31). A more definitive resonance association would be possible by showing that the phase of the wave in individual occultations matches the phase predicted for the corresponding resonance. This check on our resonance associations, as described below, is complicated by the uncertainty in the absolute radial scale that is comparable to the wavelength of the waves. Here we describe other tests based on resonance strength and observed resonance locations to check our tentative resonance associations.

4.1. Determination of theoretical resonance locations

In order to identify the potential resonances that could generate the reported wavelike structures, we updated a resonance location list with a complete mapping of all possible resonances up to 8th order with $j_1 \leqslant 50$ using converging routines based on Eqs. (6.244)–(6.246) from Murray and Dermott (1999). The following satellites were considered (in distance order to Saturn): Pan, Daphnis, Atlas, Prometheus, Pandora, Janus, Epimetheus, Mimas, Methone, Pallene, Enceladus, Tethys, Polydeuces, Dione, Rhea, Titan, Hyperion, Iapetus and Phoebe. Eq. (6.25) from Murray and Dermott (1999) provides the expression of the resonant argument Φ:

$$\Phi = j_1\lambda_s + j_2\lambda + j_3\varpi_s + j_4\varpi + j_5\Omega_s + j_6\Omega \tag{3}$$

where $\sum_{i=1}^{6} j_i = 0$, with j_i integers and $(j_5 + j_6)$ even; λ, ϖ and Ω are the mean longitude, the longitude of the pericenter and the longitude of the ascending node; the lack of subscript denotes the ring

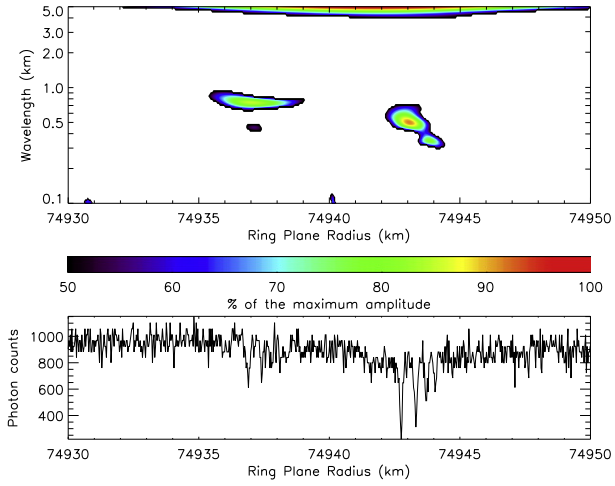

Fig. 16. WWZ wavelet power profile of structures 3 and 4, computed from α Virginis, rev. 30 individual occultation profile.

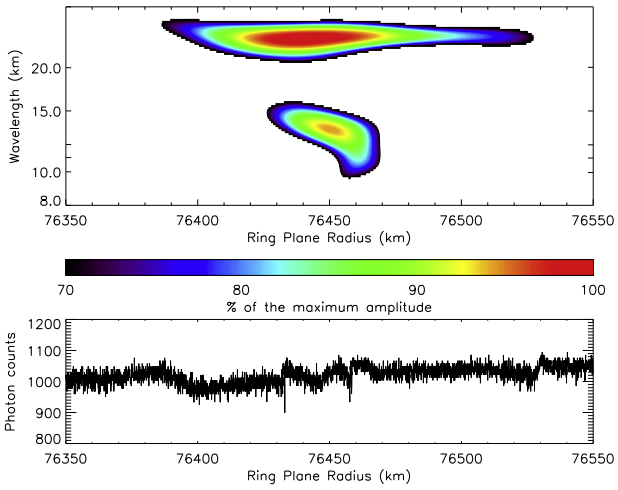

Fig. 17. WWZ wavelet power profile computed from β Centauri, rev. 85 individual occultation profile showing structures 7 and 8 coexisting at the same location. Fig. 18 gives more details about the central region where structure 9 is located.

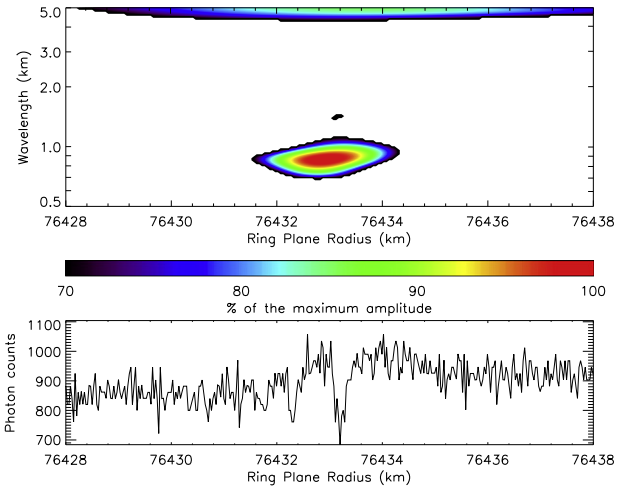

Fig. 18. WWZ wavelet power profile computed from α Virginis, rev. 34 individual occultation profile showing feature 9, propagating inward.

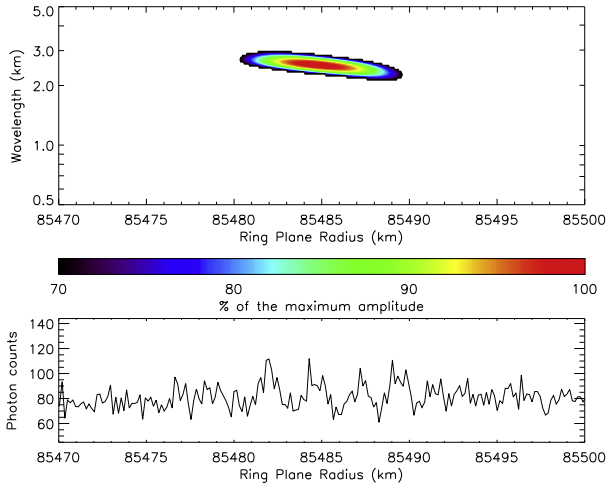

Fig. 19. WWZ wavelet power profile of structure 24, computed from ζ Orionis, rev. 47 individual occultation profile. Feature 24 is located between plateaus P5 and P6.

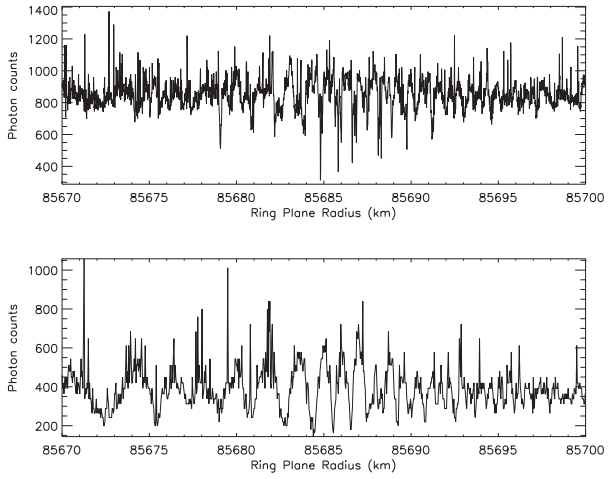

Fig. 20. Individual occultation profiles of β Centauri, rev. 64 (upper panel) and α Virginis, rev. 30 (lower panel) showing feature 27, clearly propagating outward.

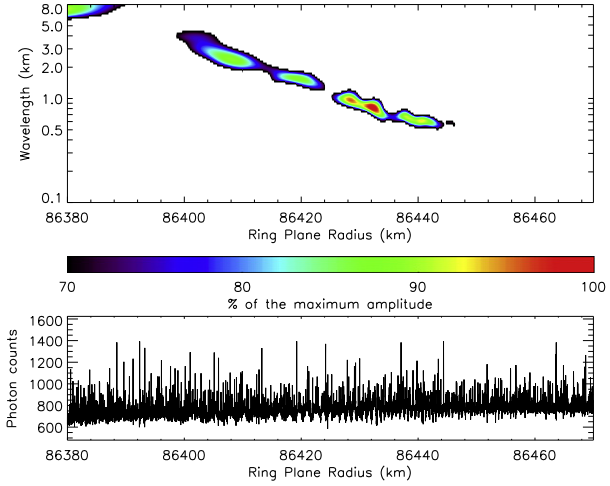

Fig. 21. Co-added WWZ wavelet power profile of structure 28, computed from individual occultation profiles. Lower panel shows the β Centauri, rev. 89 occultation profile. Structure 28 is one of the most extended feature observed in the C ring, but there is no low order resonance in its vicinity.

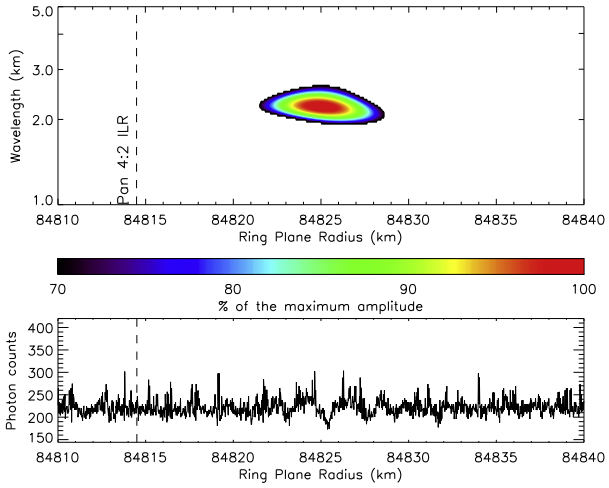

Fig. 22. WWZ wavelet power profile of feature 20, computed from β Centauri, rev. 104 individual occultation profile. Pan 4:2 ILR is at 84,814.5 km (vertical dashed line). The relatively long distance between the Pan 4:2 ILR and the wave (about the same distance as the length of the wave itself) together with a very low torque value for this resonance and an inconsistent wave source location from the feature invalidate the possibility of an association. Wave source location is outside the range of this figure, at 84,775 ± 8 km.

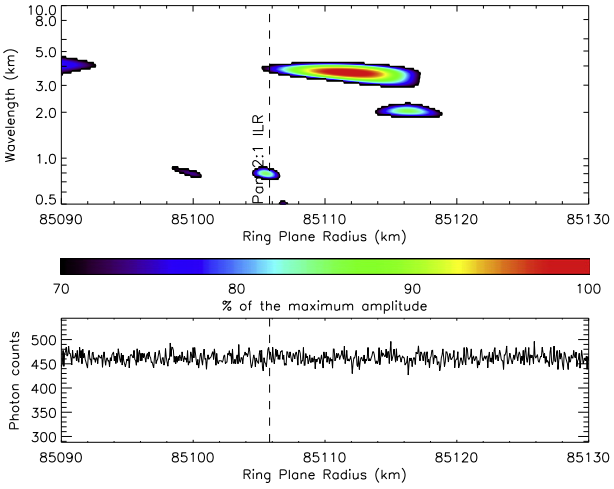

Fig. 23. WWZ wavelet power profile of structure 22, computed from β Centauri, rev. 89 individual occultation profile. Pan 2:1 ILR is at 85,105.8 km (vertical dashed line). No obvious direction of propagation can be determined from diverse occultations. Wave source location is outside the range of this figure, at 84,989 ± 20 km.

particle while subscript "*s*" denotes the disturbing satellite. Finally, the azimuthal symmetry number m, mentioned above as the number of spiral arms, is defined mathematically by $m = j_1 + j_3 + j_5$ and we also define $k = -j_3$ and $p = -j_5$.

Using the mean motion n, the epicyclic frequency κ, the vertical frequency ν and the pattern speed Ω_P defined by

$$m\Omega_P = mn_m + k\kappa_m + p\nu_m \tag{4}$$

we can express the resonant conditions by

$$m(\Omega_P - n) = j_4\kappa + j_6\nu \tag{5}$$

4.2. Resonances in the C ring

We computed the resonance locations with the highest precision available, and in particular with terms up to J_8 of the gravitational harmonics taken from Jacobson (2006) (see Table 5). Semi-major axes of Saturn's satellites were taken from Jacobson et al. (2008). In order to check for other possible resonance sources, we also calculated resonances with the synchronous orbit and with the B ring outer edge. For the synchronous orbit, we used the two periods identified by Kurth et al. (2008) in the magnetosphere rotation from early Cassini data: these periods of 10.80 h and 10.59 h vary over the course of the Cassini mission. Hedman et al. (2009) related these to the observed periods of perturbations in the D ring and the Roche Division. However, the expected main resonances with these forcing periods in the C ring are not correlated with any of the observed structures discussed here. Concerning the B ring outer edge forcing, Porco et al. (1984a) and Porco et al. (1984b) showed that the Mimas 2:1 inner Lindblad resonance is a source of perturbation of the B ring edge. Spitale and Porco (2010) recently described in detail the elements of this forced mode of the B ring edge together with three different free modes with wavenumbers 1, 2 and 3. By comparing the pattern of resonances from the B ring edge with the observed distribution of waves in the C ring, we can reject any association between B ring edge resonances and the waves reported here. Because the number of resonances can be unlimited if we go to sufficiently high order, in the next section we calculate resonance strengths to help identify associations between resonances and observed wave features.

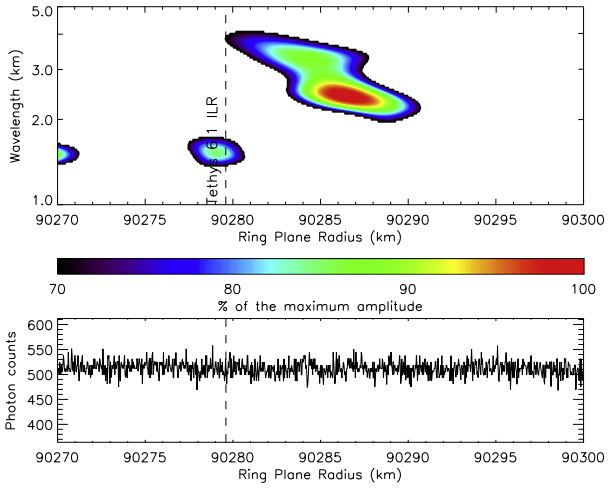

Fig. 24. WWZ wavelet power profile of wave 40, computed from β Centauri, rev. 81 individual occultation profile. Tethys 6:1 ILR is at 90,279.6 km (vertical dashed line). Its calculated strength is very low, suggesting that this is a chance association (Tiscareno et al., 2007). Wave source location is outside the range of this figure, at 90,238.5 ± 2.5 km.

4.3. Resonance strengths

Goldreich and Tremaine (1979) provided a complete derivation of the torque $T_{l,m}$ exerted by a satellite at a resonance on a uniform fluid disk in the case of inner Lindblad resonances and corotation resonances.

4.3.1. Inner Lindblad resonances

Considering a j_1: $-j_2$ inner Lindblad resonance, we have $m = j_1 + j_3 = -j_2 - j_4$. Therefore, adopting the notation of Goldreich and Tremaine (1979), we define $l = j_1$, and consider the l:$(m-1)$ inner Lindblad resonance. We then define D_L for a Lindblad resonance

$$D_L(r) = \kappa(r)^2 - m^2(n(r) - \Omega^p_{l,m})^2 \tag{6}$$

The torque can then be expressed as in Goldreich and Tremaine (1979):

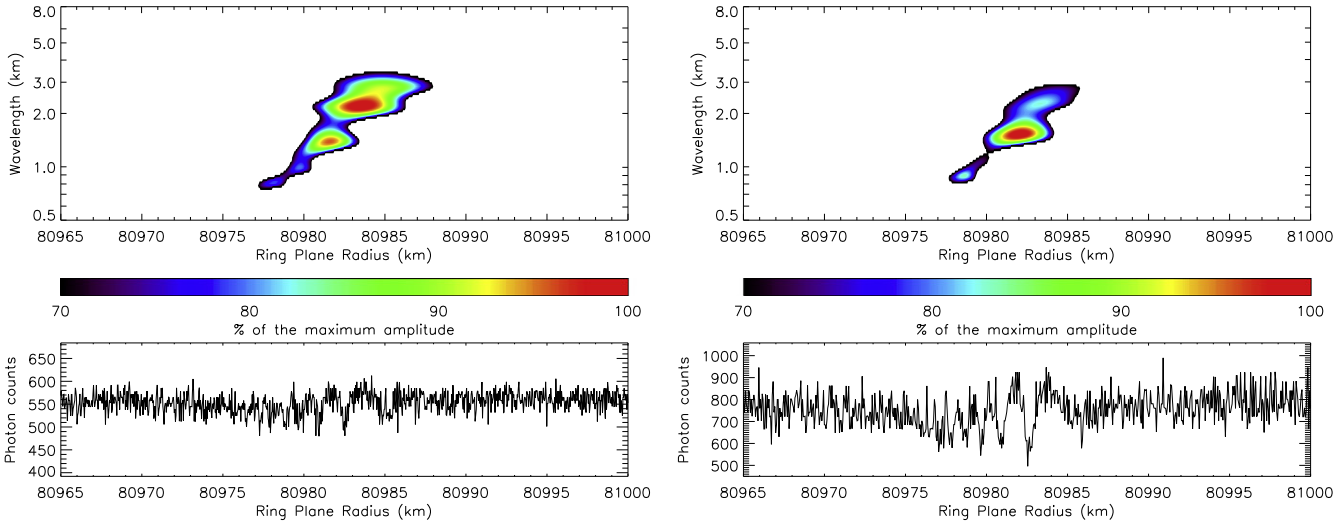

Fig. 25. WWZ wavelet power profile of structure 13, computed from individual occultation profiles of β Centauri, rev. 77 (left) and α Virginis, rev. 34 (right). Structure 13 is clearly propagating inward on both high incidence and low incidence occultations.

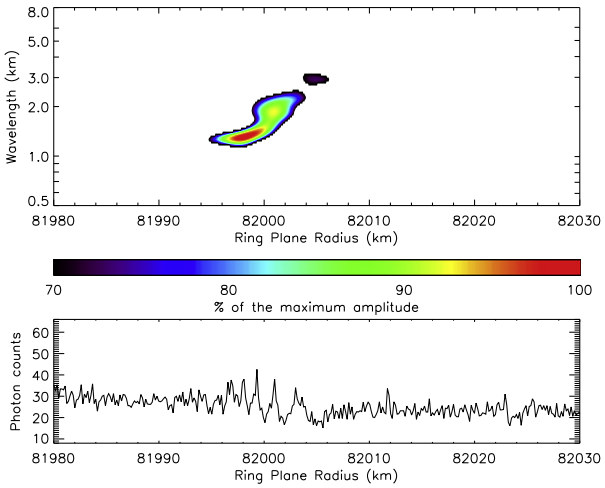

Fig. 26. WWZ wavelet power profile of feature 15, computed from co-added wavelet profiles. Lower panel shows the ζ Orionis, rev. 47 occultation profile.

$$T^L_{l,m} = -m\pi^2 \left[\sigma \left(\frac{rdD_L}{dr} \right)^{-1} \left(\frac{rd\phi^s_{l,m}}{dr} + \frac{2n(r)\phi^s_{l,m}}{n(r) - \Omega^p_{l,m}} \right)^2 \right]_{r_L} \tag{7}$$

where the Fourier components $\phi^s_{l,m}$ are evaluated from Brouwer and Clemence (1961) (ch. 15, p. 490) and Murray and Dermott (1999) Eqs. (6.244)–(6.246)) using the Keplerian approximation of $n \approx \kappa$:

$$\phi^s_{1,1} = -\frac{GM_s}{a_s} \left[b^m_{1/2}(\alpha) - \alpha \right] \tag{8}$$

$$\phi^s_{m,m} = -\frac{GM_s}{a_s} b^m_{1/2}(\alpha), \quad m > 1 \tag{9}$$

$$\phi^s_{m+1,m} = -\frac{GM_s e_s}{a_s} \left(\frac{1}{2} + m + \frac{\alpha}{2} \frac{d}{d\alpha} \right) b^m_{1/2}(\alpha), \quad m > 1 \tag{10}$$

$$\phi^s_{m+2,m} = -\frac{GM_s e_s^2}{8a_s} \left((4m^2 + m + 4) + (4m + 6)\alpha \frac{d}{d\alpha} + \alpha^2 \frac{d^2}{d\alpha^2} \right) b^m_{1/2}(\alpha), \quad m > 1 \tag{11}$$

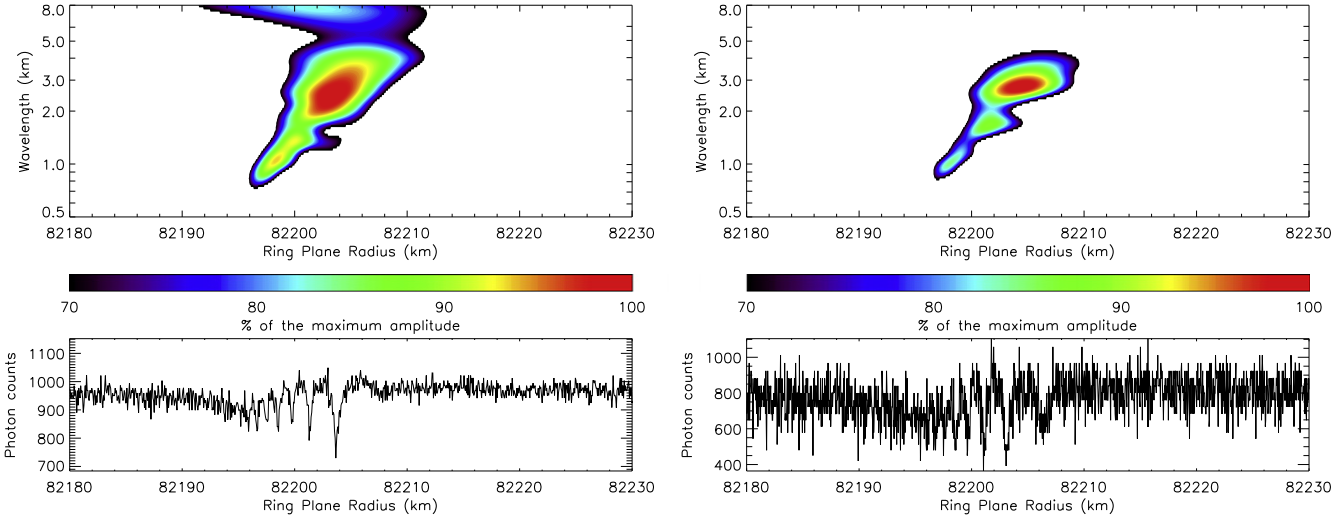

Fig. 27. WWZ wavelet power profile of structure 17, computed from co-added wavelet profiles of high-incidence angle occultations (left) and low-incidence angle occultations (right). Lower panel show the β Centauri, rev. 85 occultation profile (left) and the α Virginis, rev. 34 occultation profile (right).

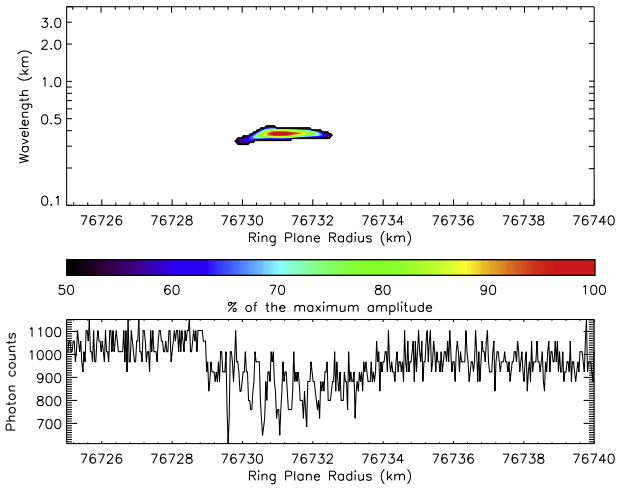

Fig. 28. WWZ wavelet power profile of structure 11, computed from α Virginis, rev. 30 individual occultation profile.

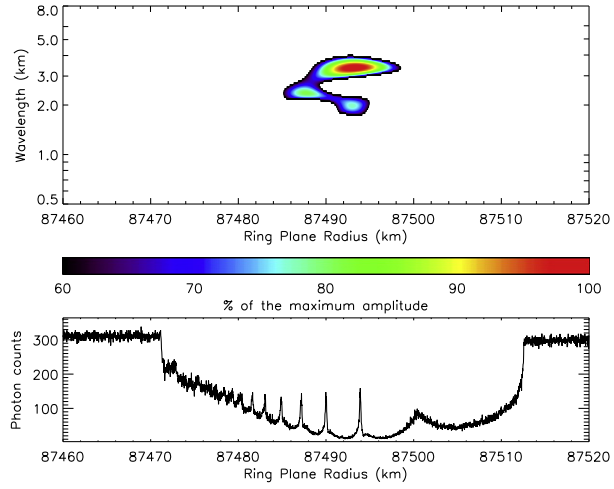

Fig. 29. WWZ wavelet power profile around Maxwell ringlet, computed from β Centauri, rev. 105 individual occultation profile. Though the structure is quite clear and prominent to the eye on the occultation profile, the WWZ profile is distorted by the relative importance of the amplitude of the highest wavelengths, hiding smaller amplitudes at the presented scale.

$$\phi^{s}_{m+3,m} = -\frac{GM_s e_s^3}{48a_s}\left((8m^3+42m^2+65m+27)+(12m^2+51m+51)\,\alpha\frac{d}{d\alpha}+(6m+15)\alpha^2\frac{d^2}{d\alpha^2}+\alpha^3\frac{d^3}{d\alpha^3}\right)b^m_{1/2}(\alpha), \quad m>1 \tag{12}$$

In these expressions, a_s and e_s are the semimajor axis and eccentricity of the perturbing satellite, $\alpha = \frac{r}{a_s}$ and $b^m_{1/2}(\alpha)$ is the Laplace coefficient defined in Eq. (13), that is calculated numerically:

$$b^m_{1/2}(\alpha) = \frac{2}{\pi}\int_0^{\pi}\frac{\cos(m\theta)\mathrm{d}\theta}{(1-2\alpha\cos\theta+\alpha^2)^{1/2}} \tag{13}$$

Even though the resonance locations have been calculated up to 8th-order, the previous development only allows the estimation of resonance strengths up to 3rd-order. In addition, Shu (1970) showed that in the absence of damping, the amplitude of a density wave grows linearly near the resonance. Lissauer and Cuzzi (1982) suggested evaluating the strength of a resonance by using the distance from resonance (located at r_L) at which the wave becomes nonlinear:

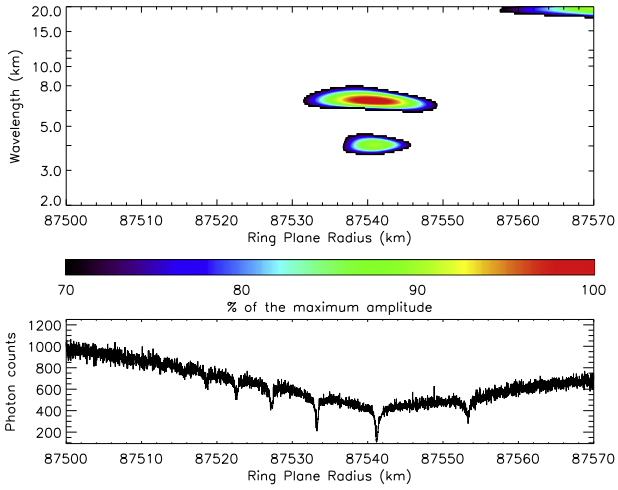

Fig. 30. WWZ wavelet power profile of Maxwell Ringlet, computed from β Centauri, rev. 64 individual occultation profile. Again, the structure is clear on the occultation profile, but the WWZ profile is distorted by the relative importance of the amplitude of the highest wavelengths.

Table 2
Ringlet signatures. Previous references are from Colwell et al. (2009b).

#	Position	Reference of existing Embedded Ringlet	Figure
1	74501-74513	ER1	Fig. 3
2	74527-74544	ER17 (new) 1 km wide	Fig. 6
3	75656-75674	ER2	Fig. 4
4	75790	ER3	
5	75970	ER6	
6	76457-76459	ER18 (new) - 2 peaks - 1 km wide	Fig. 7
7	77644-77662	ER8 (2 peaks)	Fig. 5
8	90130-90200	ER16 (Mimas 3:1 ILR)	

$$r_L X_{NL} = \frac{2\pi^2}{dD/dr}\left(-\frac{m\sigma}{r_L T^L_{l,m}}\right)^{1/2}(G\sigma)^{3/2} r_L. \tag{14}$$

In the case where the surface mass density is unknown, we compare values of $T^L_{l,m}/\sigma$ and $r_L X_{NL}\sigma^{-3/2}$. Strengths of main inner Lindblad resonances in the C ring are presented in Table 4. We should then consider possible associations with the strongest ones. Indeed, we do see some structures at the locations of the eight strongest resonances. It appears that we are only seeing structures for waves stronger than approximately the strength of the Pandora 4:2 ILR. That tends to invalidate tentative resonance association with, for example, Pan 4:2 ILR, whereas it reinforces our belief that the Mimas 4:1 ILR, the Atlas 2:1 ILR, the Mimas 6:2 ILR and the Pandora 4:2 ILR excite density waves seen respectively in structures 2, 33, 36 and 37.

For the tentative resonance associations based on the coincidence of wave feature and resonance locations (Table 4), we present the estimated values of $r_L X_{NL}$ in Table 6. Within $r_L X_{NL}$ of the wave source, undamped density waves are characterized by linear growth of the amplitude of surface mass density fluctuations, which become of order unity when $r_L X_{NL} = 1$ (Shu, 1970; Goldreich and Tremaine, 1978). Damping can reduce wave amplitude, but does not increase it, so the perturbation amplitude at a given distance from resonance should not exceed the fraction of $r_L X_{NL}$ that this distance represents. For the relatively strong Mimas 4:1 ILR, the expected distance to nonlinearity is comparable to the wave-

Table 3
Observed wavelike structures in the C ring.

Feature ID (Figure)	Inner Edge (km)	Outer Edge (km)	Direction of Decreasing Wavelength	Previous Reference	Possible Resonance Association (order)	Theoretical Resonance Location (km)	Wave Source Location (km)
1	74666	74669	Outward	Colwell et al. (2009b)			
2 (Fig. 11)	74891	74900	Outward	Rosen et al. (1991b) (a)	Mimas 4:1 ILR (3)	74891.8	74889.6 ± 1.5
3 (Fig. 16)	74935	74939	Outward	Colwell et al. (2009b)			
4 (Fig. 16)	74940	74946	Outward	Rosen et al. (1991b) (b)			
5	76013	76022	Inward	Colwell et al. (2009b)			
6	76238	76242	Outward	Colwell et al. (2009b)			
7 (Fig. 17)	76380	76500	Inward				
8 (Fig. 17)	76416	76472	Outward				
9 (Fig. 18)	76432	76435	Inward	Colwell et al. (2009b)			
10	76521	76539	Inward				
11 (Fig. 28)	76729	76732		Colwell et al. (2009b)			
12 (Fig. 12)	77524	77544	Outward	Rosen et al. (1991b) (c)	Titan -1:0 IVR BW (3)	77511.3	77509.0 ± 4.5
13 (Fig. 25)	80978	80988	Inward	Rosen et al. (1991b) (e)			
14	81018	81023	Outward				
15 (Fig. 26)	82000	82009	Inward	Colwell et al. (2009b)			
16 (Fig. 8)	82049	82061	Inward	Rosen et al. (1991b) (f)			
17 (Fig. 27)	82196	82209	Inward	Rosen et al. (1991b) (g)			
18	83628	83633	Inward	Rosen et al. (1991b) (h)			
19	84632	84644	Inward	Rosen et al. (1991b) (i)			
20 (Fig. 22)	84821	84829	Outward				
21	84857	84867	Outward				
22 (Fig. 23)	85105	85117					
23	85440	85450	Inward	Rosen et al. (1991b) (j)			
24 (Fig. 19)	85480	85491	Outward	Colwell et al. (2009b)			
25	85505	85514	Inward	Colwell et al. (2009b)			
26	85523	85533	Outward	Colwell et al. (2009b)			
27 (Fig. 20)	85677	85690	Outward	Rosen et al. (1991b) (d)			
28 (Fig. 21)	86400	86452	Outward				
29	86576	86582	Outward				
30	86584	86587	Outward				
31	86595	86601	Outward				
32 (Fig. 9)	87183	87189	Inward	Colwell et al. (2009b)			
33 (Fig. 13)	87645	87651	Outward	Colwell et al. (2009b)	Atlas 2:1 ILR (1)	87646.5	87633.4 ± 4.0
34 (Fig. 15)	88704	88716	Inward				
35	88736	88754	Outward				
36 (Fig. 14)	89889	89898	Outward		Mimas 6:2 ILR (4)	89883.3	89883.5 ± 2.0
37 (Fig. 14)	89900	89911	Outward		Pandora 4:2 ILR (2)	89894.0	89891.9 ± 1.6
38 (Fig. 10)	90143	90156	Inward				
39	90190	90210	Inward				
40 (Fig. 24)	90279	90285	Outward				

For each wavelike feature observed in the C ring, we give the edge locations, the direction of propagation when possible, previous reference (Rosen et al. (1991b) or Colwell et al. (2009b)) and possible resonance association. The final column provides wave source locations with uncertainties taking into account both intra and inter occultation uncertainties. See Section 4.3.1 for further discussion of resonance associations.
Notes: ILR : Inner Lindblad Resonance, IVR : Inner Vertical Resonance, DW : Density Wave, BW : Bending Wave.

Table 4
Strongest Inner Lindblad Resonances locations and strengths in the C ring. $r_L X_{NL}$ is the distance at which the wave becomes nonlinear. T^L_{lm} is the torque exerted on a fluid disk by a satellite at an Inner Lindblad Resonance. These quantities are depending on the surface mass density σ. Nearby structures are mentionned in the last column.

Resonance	r_L (km)	$X_{NL}\sigma^{-3/2}$ (cm^3/g$^{3/2}$)	T^L_{lm}/σ (cm^4/s^2)	Structures around
Mimas 3:1 ILR	90198.0	$2.00\ 10^{-6}$	$-2.00\ 10^{16}$	ER16 - struct 39
Prometheus 2:1 ILR	88712.9	$1.40\ 10^{-5}$	$-3.94\ 10^{14}$	R4 - struct 34 (Fig. 15)
Pandora 2:1 ILR	90167.6	$1.60\ 10^{-5}$	$-2.99\ 10^{14}$	Structure 38 (Fig. 10)
Mimas 4:1 ILR	74891.8	$5.60\ 10^{-5}$	$-6.88\ 10^{12}$	Structure 2 (Fig. 11)
Atlas 2:1 ILR	87646.5	$3.09\ 10^{-4}$	$-6.91\ 10^{11}$	Structure 33 (Fig. 13)
Pan 2:1 ILR	85105.8	$3.76\ 10^{-4}$	$-3.79\ 10^{11}$	Structure 22 (Fig. 23)
Mimas 6:2 ILR	89883.3	$4.91\ 10^{-4}$	$-1.26\ 10^{11}$	Structure 36 (Fig. 14)
Pandora 4:2 ILR	89894.0	$6.51\ 10^{-4}$	$-7.20\ 10^{10}$	Structure 37 (Fig. 14)
Prometheus 4:2 ILR	88434.5	$1.02\ 10^{-3}$	$-2.60\ 10^{10}$	

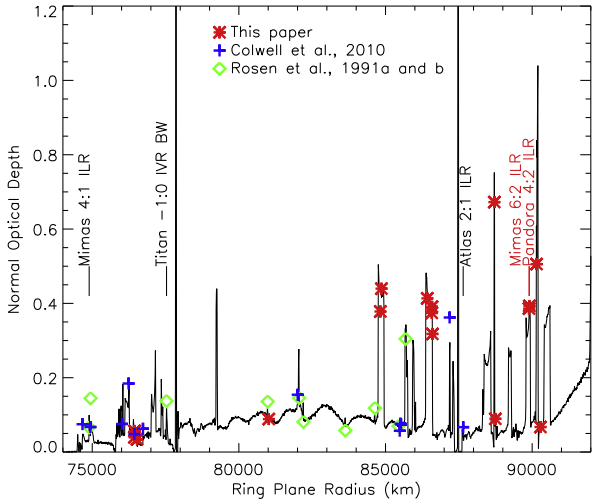

Fig. 31. Locations of the observed wavelike structures in the C ring. New developments appear in red. When available, we also show the locations of resonances that match both the wave's position and its direction of propagation. (For interpretation of the references to color in this figure legend, the reader is referred to the web version of this article.)

Table 5
Gravitational Harmonics from Jacobson et al. (2006). R^{eq}_{Saturn} = 60330 km.

Gravitational Harmonics	Value
J_2	$16290.71\ 10^{-6}$
J_4	$-935.83\ 10^{-6}$
J_6	$86.14\ 10^{-6}$
J_8	$-10.0\ 10^{-6}$

length of the first cycle. The relative amplitudes stay below 0.1 but can reach up to 0.4 later (7 km away from the wave source i.e. 4 km away from the theoretical resonance location), suggesting significant damping but reinforcing the association of the resonance with the observed wave. For the Mimas 6:2 ILR ($r_L X_{NL}$ = 66.2 km), we measure a relative perturbation amplitude of 0.21 at the location corresponding to $0.02 R_L X_{NL}$. The excitation of the Mimas 6:2 ILR alone could not explain this amplitude, and our confidence in this association is weakened. The Pandora 4:2 ILR overlaps the Mimas 6:2 ILR, preventing us from evaluating amplitudes due to this wave alone. For the Atlas 2:1 ILR ($r_L X_{NL}$ = 2.79 km), the predicted distance to non-linearity is comparable to the wavelength. The maximum observed relative amplitude is 0.13, which could be explained by damping.

4.4. Wave dispersion relation

Eq. (10) from Rosen et al. (1991a) gives the dispersion of the wavelength $\lambda(r)$ in the case of a density wave associated with an l:($m-1$) Lindblad resonance:

$$\sigma = \frac{|r - r_L|\lambda(r)}{4\pi^2 G r_L}\mathcal{D}_L(r) \tag{15}$$

where (Marley and Porco, 1993):

$$\mathcal{D}_L(r) = \left(3(m-1)n(r)^2 + J_2\left(\frac{R_{Saturn}}{r_L}\right)^2\left(\frac{21}{2} - \frac{9}{2}(m-1)\right)n(r)^2\right) \tag{16}$$

The azimuthal symmetry number m is known for waves that can be associated with a given resonance, but for waves whose forcing is not known, m is also unknown, and Eq. (15) may not be valid if the structure is not due to an inner Lindblad or vertical resonance. However, modeling outward propagating waves as density waves and inward propagating waves as bending waves allows one to determine $\frac{\sigma}{m-1}$ for which we considered r_L to be the location of the beginning of the wave, and λ the wavelength of peak power. The second term of Eq. (16) being very small compared to the first one in the case where $m > 1$, we have:

$$\frac{\sigma}{m-1} \approx \frac{3|r - r_L|\lambda(r)n(r)^2}{4\pi^2 G r_L}, m > 1 \tag{17}$$

5. Discussion

Thanks to the resonance associations from Section 3, we can extract mean surface mass densities at these resonance locations in

Table 6
Optical depth τ, derived surface mass densities σ, mass extinction coefficients κ, wave damping length ξ_d, and vertical thickness H of the rings of wavelike structures with associated resonance in the C ring and their resonant argument parameters (Section 4.1).

Resonance (order)	Figure	$r_L(r_V)$ (km)	m	($j_1, j_2, j_3, j_4, j_5, j_6$)	σ (g cm^{-2})	τ	κ (cm^{2}g^{-1})	ξ_d	H (m)	$r_L X_{NL}$ (km)
Mimas 4:1 ILR (3)	Fig. 11	74891.8	2	(4,−1,−2,−1,0,0)	0.58 ± 0.09	0.08	0.13 ± 0.03	4.23	4.1 ± 1.0	1.85
Titan −1:0 IVR BW (3)	Fig. 12	77511.3	1	(−1,0,1,0,1,−1)	0.60 ± 0.09	0.10	0.17 ± 0.03	5.14	5.6 ± 1.4	
Atlas 2:1 ILR (1)	Fig. 13	87646.5	2	(2,−1,0,−1,0,0)	0.22 ± 0.03	0.04	0.19 ± 0.04	5.42	1.9 ± 0.4	2.79
Mimas 6:2 ILR (4)	Fig. 14	89883.3	3	(6,−2,−3,−1,0,0)	1.31 ± 0.20	0.37	0.28 ± 0.06	6.61	2.4 ± 0.6	66.2
Pandora 4:2 ILR (2)	Fig. 14	89894.0	3	(4,−2,−1,−1,0,0)	1.42 ± 0.21	0.37	0.26 ± 0.05	6.69	2.4 ± 0.6	99.0

the C ring. Table 6 reports mean surface mass densities and mean mass extinction coefficients $\left(\kappa_{mean} = \frac{\tau}{\sigma_{mean}}\right)$.

For a differential particle size distribution $n(a) = n_0\left(\frac{a_0}{a}\right)^q$ with $a_{min} \leqslant a \leqslant a_{max}$, the mass extinction coefficient is defined by

$$\kappa = \frac{\tau}{\sigma} = \frac{\int_{a_{min}}^{a_{max}} n(a)S(a)\mathrm{d}a}{\int_{a_{min}}^{a_{max}} n(a)m(a)\mathrm{d}a} = \frac{3(4-q)}{4(3-q)}\left(\frac{a_{max}^{3-q} - a_{min}^{3-q}}{a_{max}^{4-q} - a_{min}^{4-q}}\right)\rho^{-1} \quad (18)$$

where ρ is the mass density of the particles. Using the power law index estimated by Zebker et al. (1985) for the C ring ($q \sim 3.1$), we find $\kappa \propto \frac{1}{a_{max}}$: the biggest particles are smaller when κ is higher. The mass extinction coefficient is an integrated property of the particle size distribution and varies across the C ring.

For the tentative resonance associations, we derived values of κ between 0.13(±0.03) (for the Mimas 4:1 ILR) and 0.28(±0.06) cm^2 g^{-1} (for the Mimas 6:2 ILR). In addition, assuming the other wavelike features are spiral density or bending waves with $m > 1$, $\frac{\sigma}{m-1}$ is a lower limit of σ while $\kappa(m-1)$ is an upper limit of κ at that location. We present these limit values in Table 7: values for $\kappa(m-1)$ are found between 0.004 and 0.63 cm^2 g^{-1}. We present mass extinction coefficient results in Fig. 32. Our maximal estimated mass extinction coefficient $\kappa(m-1) = 0.63$ cm^2 g^{-1} (though κ could be smaller than this value if $m \gg 1$) is much higher than the A ring values (0.01–0.02 cm^2 g^{-1}) and the Cassini Division values (0.07 – 0.12 cm^2 g^{-1} from Colwell et al. (2009a)), even if in some locations the upper limit on κ may be lower than in the A ring. We notice that the highest values of mass extinction coefficient limits are mainly found in plateau regions. Therefore, particle sizes may be smaller in these plateaus. This result is in accordance with a recent study from Colwell et al. (2010). Finally, in contrast to the A ring and the Cassini Division where the mass extinction coefficient is fairly constant, it appears to increase with radius along the C ring (assuming there is not a systematic trend of the m values). We next turn our attention to the viscosity and thickness of the ring.

The wave damping length is defined by (Tiscareno et al., 2006):

Table 7
Optical depth τ, and constraints on derived surface mass densities σ and mass extinction coefficients κ of wavelike structures with associated resonance in the C ring.

r (km)	Structure	Figure	$\frac{\sigma}{m-1}$ (g cm^{-2})	τ	$\kappa \times (m-1)$ (cm^{2}g^{-1})
74666	1		5.83	0.04	0.006
74923	3	Fig. 16	0.48	0.05	0.005
74939	4	Fig. 16	0.28	0.13	0.46
76022	5		3.88	0.04	0.011
76234	6		0.30	0.15	0.50
76435	9	Fig. 17	0.33	0.06	0.19
76539	10		9.21	0.03	0.004
76729	11		0.14	0.07	0.52
80988	13	Fig. 25	1.17	0.13	0.11
81018	14		0.40	0.10	0.25
82010	15	Fig. 26	1.42	0.14	0.10
82061	16	Fig. 8	2.54	0.28	0.11
82209	17	Fig. 27	1.73	0.13	0.08
83633	18		0.45	0.10	0.22
84644	19		1.35	0.11	0.08
84814	20	Fig. 22	1.97	0.44	0.22
84857	21		1.12	0.42	0.38
85450	23		0.55	0.07	0.13
85473	24	Fig. 19	2.77	0.07	0.03
85514	25		0.64	0.07	0.11
85677	27	Fig. 20	0.62	0.29	0.46
86400	28	Fig. 21	2.35	0.47	0.20
86576	29		0.59	0.38	0.63
87189	32	Fig. 9	0.47	0.15	0.33
88736	35		1.77	0.07	0.04
90156	38	Fig. 10	1,94	0.67	0.35
90279	40	Fig. 24	1,14	0.06	0.06

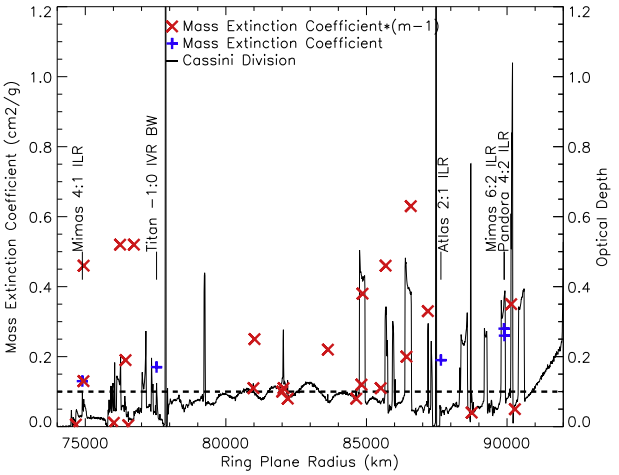

Fig. 32. Mass extinction coefficient limit values. Actual mass extinction coefficient values, calculated at the associated resonance locations, are displayed in blue while upper limits of mass extinction coefficient, estimated from $\kappa \times (m-1)$, are shown in red. (For interpretation of the references to color in this figure legend, the reader is referred to the web version of this article.)

$$\xi = \left(\frac{\mathcal{D}_L r_L}{2\pi G\sigma_0}\right)^{1/2} \frac{r - r_L}{r_L} \quad (19)$$

Using the definition of the ring viscosity given by Shu (1984),

$$\eta \approx \frac{9}{7n\xi^3}\sqrt{\frac{(2\pi G\sigma)^3 r_L}{\mathcal{D}_L}} \quad (20)$$

we derive the vertical thickness of the rings H as defined by Tiscareno et al. (2007):

$$H = \frac{1}{n}\sqrt{\frac{2\eta n}{\tau}(1+\tau^2)} \quad (21)$$

Values of the wave damping length and of the vertical thickness of the rings for tentative resonance associations are reported in Table 6. We find that the C ring has a height of 1.9(±0.4)–5.6(±1.4) m, which is consistent with the vertical thickness of the Cassini Division, between 3 and 20 m (Tiscareno et al., 2007; Colwell et al., 2009a.

Finally, using the limits of the range of the mass extinction coefficients (derived from associated resonances), and assuming a uniform value of this coefficient along the C ring, we can constrain the mass of the C ring between 3.7(±0.9) × 10^{16} kg (obtained from the tentative association with Atlas 2:1 ILR) and 7.9 (±2.0) × 10^{16} kg, which could be represented by a satellite (with a density of 400 kg m^{-3} close to the density of Pan and Atlas) with a radius of 28.0(±2.3) km to 36.2(±3.0) km (a little bigger than Pan or Atlas). For comparison, Spilker et al. (2004) estimated the A ring to be equivalent to a 110 km radius icy moon and Charnoz et al. (2010) produced numerical simulations generating a 1.5 × 10^{18} kg A ring with a similar density (equivalent to a 96 km-radius moon). Colwell et al. (2009a) estimated the Cassini Division mass to 3.1 × 10^{16} kg, ramp excluded.

Zebker et al. (1985) estimated values for the upper size cutoffs of the particle size distribution between 2.4 and 5.3 m in the C ring, whereas they measured 7.5 m in the Cassini Division and from 5.0 to 11.2 m in the A ring, based on differential optical depths at radio wavelengths. Colwell et al. (2009a) interpreted the higher mass extinction coefficients in the Cassini Division compared to the A ring as evidence that the upper size cutoff in the Cassini Division is 3–5 times smaller than that in the A ring. Our mass extinction coefficients from the handful of C ring waves with a reasonably firm resonance identification are more in line with those in the

Cassini Division than those in the A ring. Though we do not know the wave pattern number m for most waves, taken all together the waves in the C ring suggest that the mass extinction coefficient may be larger than in the Cassini Division and that the particle size distribution has an even smaller upper limit. We can therefore imagine that the particles composing these different rings have either different origins or that their size distributions are not primordial and have evolved differently.

The highest mass extinction coefficients in the C ring appear to be in the plateaus. The plateaus themselves are of unknown origin, and the different size distributions could be a clue to their origin or evolution.

The C ring and Cassini Division are generally similar in a number of respects (color, optical depth, and, apparently, particle size distribution), but are separated by the broad and massive B ring. If they do not have the same age and origin, the C ring and Cassini Division may have a common mode of origin that has lead to their gross overall similarities. Like the origin of the ring itself, the origins of most of the wavelike structures in the C ring remain unresolved. Although many of the waves have been observed from the Voyager epoch to the Cassini epoch and their structures appear very similar to density and bending waves, most do not appear to share the prominent association with strong resonances with Saturn's moons that characterize their counterparts in the A ring and Cassini Division. Explaining these structures and their sources is a necessary step in understanding the complexity and variety of the rings' evolution.

Acknowledgments

This material is based upon work supported by the National Aeronautics and Space Administration under Grant No. NNX10AF20G issued through the Cassini Data Analysis Program. We are indebted to J.N. Spitale and M.S. Tiscareno for valuable suggestions and thorough reviews that improved the quality of the manuscript significantly. We also thank J.H. Cooney and T. Becker for their helpful comments.

References

Brouwer, D., Clemence, G.M., 1961. Methods of Celestial Mechanics. Academic Press, New York.
Charnoz, S., Salmon, J., Crida, A., 2010. The recent formation of Saturn's moonlets from viscous spreading of the main rings. Nature 465, 752–754.
Colwell, J.E., Esposito, L.W., Sremčević, M., Stewart, G.R., McClintock, W.E., 2007. Self-gravity wakes and radial structure of Saturn's B ring. Icarus 190, 127–144.
Colwell, J.E., Cooney, J.H., Esposito, L.W., Sremčević, M., 2009a. Density waves in Cassini UVIS stellar occultations. 1. The Cassini Division. Icarus 200, 574–580.
Colwell, J.E., Nicholson, P.D., Tiscareno, M.S., Murray, C.D., French, R.G., Marouf, E.A., 2009b. The structure of Saturn's rings. In: Dougherty et al. (2009), Saturn from Cassini–Huygens, pp. 375–412.
Colwell, J.E., Esposito, L.W., Jerousek, R.G., Sremčević, M., Pettis, D., Bradley, E.T., 2010. Cassini UVIS stellar occultation observations of Saturn's rings. Astron. J. 140, 1569–1578.
Dougherty, M.K., Esposito, L.W., Krimigis, S.M. (Eds.), 2009. Saturn from Cassini–Huygens. doi:10.1007/978-1-4020-9217-6.
Esposito, L.W. et al., 2004. The Cassini Ultraviolet Imaging Spectrograph Investigation. Space Sci. Rev. 115, 299–361.
Esposito, L.W., Colwell, J.E., McClintock, W.E., 1998. Cassini UVIS observations of Saturns rings. Planet. Space Sci. 46, 1221–1235.
Foster, G., 1996. Wavelets for period analysis of unevenly sampled time series. Astron. J. 112, 1709–1729.
French, R.G. et al., 1993. Geometry of the Saturn system from the 3 July 1989 occultation of 28 SGR and Voyager observations. Icarus 103, 163–214.
Goldreich, P., Tremaine, S.D., 1978. The formation of the Cassini Division in Saturn's rings. Icarus 34, 240–253.
Goldreich, P., Tremaine, S., 1979. The excitation of density waves at the Lindblad and corotation resonances by an external potential. Astrophys. J. 233, 857–871.
Goldreich, P., Tremaine, S., 1982. The dynamics of planetary rings. Ann. Rev. Astron. Astrophys. 20, 249–283.
Greenberg, R., Brahic, A. (Eds.), 1984. Planetary rings. Tucson, University of Arizon Press, Arizona, 801p.
Hedman, M.M., Burns, J.A., Tiscareno, M.S., Porco, C.C., 2009. Organizing some very tenuous things: Resonant structures in Saturn's faint rings. Icarus 202, 260–279.
Jacobson, R.A. et al., 2006. The gravity field of the saturnian system from satellite observations and spacecraft tracking data. Astron. J. 132, 2520–2526.
Jacobson, R.A., Spitale, J., Porco, C.C., Beurle, K., Cooper, N.J., Evans, M.W., Murray, C.D., 2008. Revised orbits of Saturn's small inner satellites. Astron. J. 135, 261–263.
Kurth, W.S., Averkamp, T.F., Gurnett, D.A., Groene, J.B., Lecacheux, A., 2008. An update to a saturnian longitude system based on kilometric radio emissions. J. Geophys. Res. (Space Phys.) 113 (12), 5222.
Lissauer, J.J., Cuzzi, J.N., 1982. Resonances in Saturn's rings. Astron. J. 87, 1051–1058.
Marley, M.S., Porco, C.C., 1993. Planetary acoustic mode seismology – Saturn's rings. Icarus 106, 508–524.
Murray, C.D., Dermott, S.F., 1999. Solar System Dynamics. Springer, Berlin.
Nicholson, P.D., Hedman, M.M., Cassini VIMS Team 2010. A Crack in the C Ring? In: AAS/Division for Planetary Sciences Meeting Abstracts #42. Vol. 42 of Bulletin of the American Astronomical Society, p. 981.
Porco, C., Danielson, G.E., Goldreich, P., Holberg, J.B., Lane, A.L., 1984a. Saturn's nonaxisymmetric ring edges at 1.95 R(s) and 2.27 R(s). Icarus 60, 17–28.
Porco, C., Nicholson, P.D., Borderies, N., Danielson, G.E., Goldreich, P., Holberg, J.B., Lane, A.L., 1984b. The eccentric saturnian ringlets at 1.29 R(s) and 1.45 R(s). Icarus 60, 1–16.
Rosen, P.A., Lissauer, J.J., 1988. The Titan-1:0 Nodal bending wave in Saturn's Ring C. Science 241, 690–694.
Rosen, P.A., Tyler, G.L., Marouf, E.A., 1991a. Resonance structures in Saturn's rings probed by radio occultation. I – Methods and examples. Icarus 93, 3–24.
Rosen, P.A., Tyler, G.L., Marouf, E.A., Lissauer, J.J., 1991b. Resonance structures in Saturn's rings probed by radio occultation. II – Results and interpretation. Icarus 93, 25–44.
Shu, F.H., 1970. On the density-wave theory of galactic spirals. II. The propagation of the density of wave action. Astrophys. J. 160, 99–112.
Shu, F.H., 1984. Waves in planetary rings. In: Greenberg and Brahic, 1984, IAU Colloq. 75: Planetary Rings, pp. 513–561.
Spilker, L.J., Pilorz, S., Lane, A.L., Nelson, R.M., Pollard, B., Russell, C.T., 2004. Saturn A ring surface mass densities from spiral density wave dispersion behavior. Icarus 171, 372–390.
Spitale, J.N., Porco, C.C., 2010. Detection of free unstable modes and massive bodies in Saturn's outer B ring. Astron. J. 140, 1747–1757.
Tiscareno, M.S., Nicholson, P.D., Burns, J.A., Hedman, M.M., Porco, C.C., 2006. Unravelling temporal variability in Saturn's spiral density waves: Results and predictions. Astrophys. J. 651, L65–L68.
Tiscareno, M.S., Burns, J.A., Nicholson, P.D., Hedman, M.M., Porco, C.C., 2007. Cassini imaging of Saturn's rings. II. A wavelet technique for analysis of density waves and other radial structure in the rings. Icarus 189, 14–34.
Tiscareno, M.S., Hedman, M.M., Burns, J.A., Weiss, J.W., Porco, C.C., 2009. Saturn's A ring has no inner edge. In: AAS/Division for Planetary Sciences Meeting Abstracts #41. Vol. 41 of AAS/Division for Planetary Sciences Meeting Abstracts, p. #25.04.
Torrence, C., Compo, G.P., 1998. A practical guide to wavelet analysis. Bull. Am. Meteorol. Soc. 79, 61–78.
Zebker, H.A., Marouf, E.A., Tyler, G.L., 1985. Saturn's rings – Particle size distributions for thin layer model. Icarus 64, 531–548.